International Journal of Applied Ceramic Technology

Research Article

Impact of thermal oxidation on morphological characteristics of cordierite and attapulgite substrate materials

Submission ID 4ba71d32-dd19-4132-88f5-a5fe7bd10ad8

Submission Version Revision 1

PDF Generation 28 May 2025 12:57:09 EST by Atypon ReX

Authors

Bowen Zhao
Corresponding Author
Submitting Author

ORCiD
https://orcid.org/0009-0005-2343-5044

Affiliations
- Lanzhou University of Technology, Lanzhou 730050, China

Tao Peng

Affiliations
- Gansu Research Institute of Light Industry Co., Ltd., Lanzhou 730099, China

Xiaoxue Zhang

Affiliations
- Gansu Research Institute of Light Industry Co., Ltd., Lanzhou 730099, China

Junpeng Li

Affiliations
- Lanzhou University of Technology, Lanzhou 730050, China

Ye Liu

Affiliations
- Institute for Transport Studies, University of Leeds, Leeds, LS2 9JT, UK

Additional Information

Keywords

Diesel engine; Attapulgite; Heat recovery; Morphology; Soot oxidation

Fixed Keywords

oxidation

substrates

thermal analysis

Files for peer review

All files submitted by the author for peer review are listed below. Files that could not be converted to PDF are indicated; reviewers are able to access them online.

Name	Type of File	Size	Page
Revised Manuscript clean and final version.docx	Main Document - MS Word	3.5 MB	Page 4
Revised Manuscript with changes Marked.docx	Main Document - Tracked Changes	3.5 MB	Page 44
Authors' Response to Reviewers' Comments.docx	Author Response	18.3 MB	Page 84

Impact of thermal oxidation on morphological characteristics of cordierite and attapulgite substrate materials

Bowen Zhao[a]*, Tao Peng[b], Xiaoxue Zhang[b], Junpeng Li[a], Ye Liu[c]*

[a]Lanzhou University of Technology, Lanzhou 730050, China

[b]Gansu Research Institute of Light Industry Co., Ltd., Lanzhou 730099, China

[c]Institute for Transport Studies, University of Leeds, Leeds, LS2 9JT, UK

*Corresponding Authors: zhaobw@lut.edu.cn; Y.Liu8@leeds.ac.uk

Abstract

The diesel particulate filter (DPF) is one of the most effective devices for reducing particulate emission, where the continuous DPF regeneration is necessary for maintaining filter efficiency. There is currently a lack of investigation on the effect of thermal oxidation on morphological characteristics of substrate materials. In this study, the cordierite (Cord) and attapulgite (ATP) powders were mixed with CeO_2, serving as substrate and catalyst, respectively. The soot particles were collected from a heavy-duty diesel engine. Through the thermal oxidation from 450 to 650 ℃, it was found that the special fibrous or rod-like structure of ATP produced more pore volume and surface area, as well as an efficient heat recovery mechanism after thermal oxidation. The block-like structure of Cord only acted as a substrate, maintaining its intact crystalline structure during thermal oxidation. Notably, the oxidation reactivity of ATP/CeO_2/Soot was higher than Cord/CeO_2/Soot because the ATP generated more catalyst active sites and sufficient contact area for the soot-oxygen-CeO_2 reaction. This study expands the potential application of ATP as DPF substrate material.

Keywords: Diesel engine; Attapulgite; Heat recovery; Morphology; Soot oxidation

1. Introduction

Diesel particulate matter contributes to serious environmental issues including haze and photochemical smog. The diesel particulate filter (DPF) showed significant potential for particulate reduction and typically achieving filtration efficiencies exceeding 95% [1]. In DPF, the soot particle layer must be removed by regeneration either periodically or continuously to prevent the increase of backpressure and fuel consumption [2, 3]. The active regeneration involved by soot particles burning above 550 ℃ in exhaust. The DPF regeneration process was a complex and endothermic reaction process. The catalyst substrate structural characteristics were affected by heat release during regeneration [4-6].

In order to improve active regeneration performance of DPF, the thermal management for parallel channels has been widely researched [7,8]. Yu et al. [9] reported that the DPF heat transfer properties depend on the heat capacitance ratio and the hydraulic parameters. With the decrease of the DPF substrate thickness, the speed of the temperature front was improved. Fang et al. [10] suggested that the peak substrate temperature of substrate material was affected by regeneration temperatures, while decreasing exhaust flow rate and improving regeneration temperature resulted in higher peak substrate temperature and maximum temperature gradients. Lee et al. [11] reported that the thermal capacity and heat transfer rate of DPF parallel channels were influenced by oxygen concentration and maximum wall temperature. Higher oxygen concentration led to thermal failure, while higher soot deposition with the higher

regeneration temperature produced the best regeneration performance [12]. Meng et al. [13,14] cordierite structure could change to some extent at high temperature, which affected the filtration efficiency. High temperature airflow and microporous expansion enhanced particle penetration.

The materials used for manufacturing DPF played an important role in regeneration process [8,15]. The channels of DPF consist of porous substrate material included cordierite, silicon carbide, acicular mullite, aluminum titanate, metal foams and fibers [16]. Cordierite (abbreviated hereafter as Cord), derived from a mixture containing clay [$Mg_2Al_4SiO_{18}$], served as the primary component of DPF catalyst substrate. It was reported that the Cord is known to form at high temperature sintering method, which has a dense microstructure with evenly distributed grains and few small pores [17]. The Cord had favorable thermal expansion coefficient and resistance to cracking from material fatigue, and an excellent thermal shock resistance [18-21]. Xu et al. [22] mentioned that the flow uniformity and pressure drop of DPF channels were affected by the permeation resistance of the Cord substrate material. It has been confirmed that cordierite mixed with a small amount of CeO_2 showed unique oxygen storage capacity, which was recommended as a suitable catalytic converter for regeneration [23-25]. Zeng et al. [26] found that CeO_2 nanoparticles could provide a higher surface area without any heat treatment. The CeO_2 could be uniformly distributed across the interconnected pores of cordierite. Liu et al. [27] reported that the incorporation of CeO_2 facilitated the phase transformation of Cord, increasing permeability and larger pore sizes. In addition, to promote solid–solid interaction, some

new morphologies of ceria-based catalyst have been proposed, such as fibers, sticks, flakes, cubes, rods and stars. Among them, fibrous morphology was the best one for passive regeneration [28]. Zhang et al. [29] suggested that aluminum borate whiskers with cilia-like microstructure improved soot capture ability and low-temperature catalytic oxidation ability of soot. The filter efficiency, trapped soot particle distribution and catalyst content were affected by porous media in substrate material [30,31].

To improve temperature resistance and regeneration performance, researchers have continuously explored new carrier materials. At present, research on DPF substrate material was mainly focused on structural parameters [32-36]. Attapulgite (hereafter abbreviated as ATP) is a type of hydrated magnesium-aluminum silicate mineral [$(H_2O)_4(Mg,Al,Fe)_5(OH)_2Si_8O_{20}\cdot 4H_2O$] [22]. ATP has been widely used as catalyst substrate material because of its larger surface area, pore volume and thermal stability [37,38]. Cao et al. [39] demonstrated that the CuO catalyst doped over ATP showed good catalytic activity and thermal stability for CO oxidation. Zhu et al. [40] found that TiO_2 coated on ATP has been utilized to remove gaseous carbon disulfide (CS_2) from air. Larger surface area of ATP improved CS_2 removal efficiency. Additionally, ATP was employed as a catalyst support to remove diesel engine NOx emission, showing excellent performance [41].

The most direct influence on soot oxidation behavior is the contact point, which is determined by substrate material. However, there is a lack of investigation on structural changes of catalyst substrate material during thermal oxidation treatment. The larger surface area and pore volume of ATP were favorable for soot particle

deposition and catalytic reaction. Therefore, this study aimed to comprehensively evaluate the effect of thermal oxidation on morphological characteristics of Cord and ATP using various characterization techniques. Four types of ATP and Cord substrates were tested by thermal oxidation. The results revealed the impact of thermal oxidation on morphology, surface structure, crystalline structure and graphitization degree of substrate material. Additionally, the catalytic performances of CeO_2 coated on ATP and Cord were evaluated.

2. Experimental methodology

2.1 Experiment material

In present study, for thermal oxidation reaction, CeO_2 powder (99.99% purity, Sinopharm Chemical Reagent Co. Ltd., Shanghai, China) was selected as catalyst. It was reported that the CeO_2 catalyst doped over Cord exhibited significant oxygen storage capacity, appropriate porosity, flexural strength and thermal expansion coefficient [42,43]. The ATP powder, characterized by an average crystal diameter of 40~50 nm and honeycomb pore dimension measuring 0.38 nm × 0.63 nm, was produced from Gansu RongWan Science and Technology Co., Ltd. Cord powder was produced from Henan Hengyang Refractory Materials Co., Ltd., Henan, China. The ATP and Cord clays were used without any further purification, which were used as the porous substrates in this study. The ATP and Cord powders were selected based on their mesh sizes, specifically 200 mesh (particle diameter: 74 μm) and 325 mesh (particle diameter: 46 μm), respectively. A series of ATP/CeO_2 or Cord/CeO_2 samples were obtained so-called tight-contact mode by a pestle to grind carrier for 5 min, which

was synthesized by mechanical grinding method. The mass ratio of substrate and CeO_2 was prepared by 1/1 (100 mg/100 mg).

The most direct influence on soot oxidation behavior was the contact point between soot particle, catalyst and substrate, which was difficult to research in molded DPF filter [44,45]. Some researchers have evaluated catalyst activity towards soot oxidation by powder form due to its superior dispersion [46,47]. The powdered Cord and ATP as substrate material increased the effective contact area between soot particles and catalyst. The interaction between the microstructure of catalyst substrate and thermal oxidation could also be observed visually. In order to figure out the effect of mechanical grinding on particle sizes of ATP and Cord, the effect of mechanical grinding on particle size were analyzed by laser particle size distribution instrument (BT-9300H), which has been listed in Fig. 1. It was shown that the volume mean diameter of ATP/CeO_2 and Cord/CeO_2 decreased by 1-2 μm after mechanical grinding. The particle size of the Cord and ATP samples remained unchanged, which had little effect on the experimental results. The substrate/CeO_2 samples are named as ATP200/CeO_2, ATP325/CeO_2, Cord200/CeO_2 and Cord 325/CeO_2.

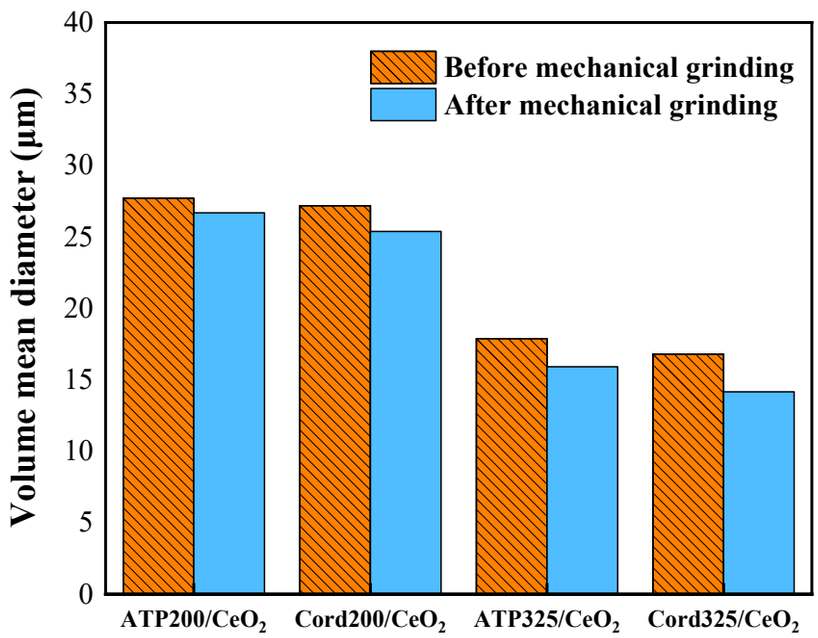

Fig. 1. Volume diameter of substrate/catalyst samples before and after mechanical grinding.

A heavy-duty diesel engine was employed to generate soot particles under steady-state condition (1500 r/min and 200 Nm). A comprehensive description of engine setup along with the sampling system is illustrated in Fig. 2. The engine specifications are detailed in Table 1. Soot particles were collected from the raw exhaust using 47 mm quartz fiber filters (2500QRT-UP, PALL) equipped with an automated filter support. The quartz fiber filters exhibited a precision of 0.3 μm with an aerosol retention rate of 99.9%. The sampling temperature was maintained at 55 ± 3 °C, with sampling duration of 90 min and sample flow rate of 1 L/s. In order to get enough samples for further analysis, the sampling time was controlled at 2 hours or longer. Subsequently, the particles attached to the filter paper surface were carefully scraped off from the paper filters. During this process, the filter paper was guaranteed not to be damaged, and the interference of filter paper could be removed. To prevent atmospheric moisture from

affecting the samples, the soot particle samples were stored in a desiccator after each measurement [48]. There pre-treatments like ultrasonic wave treatment and centrifugal separation in dichloromethane solvent were not employed in this study [49].

In order to simulate soot oxidation real DPF channels, the powdered soot particle and substrate/catalyst sample were mixed by gently shaking with a vortex mixer for 2 min at a weight ratio of 1:10 (10 mg of soot particle to 100 mg of substrate/catalyst), which was named as loose-contact mode and be employed in many literatures [50-53]. When the soot particles trapped inside the DPF channels, the oxidation rate of soot was related to the effective contact area of the catalyst [54,55]. The experimental method employed in this study revealed the difference of contact conditions between Cord, ATP, CeO_2 and soot particles. The key influencing the catalytic performance was the porosity in the DPF substrate [56,57]. The powdered soot-substrate mixtures could provide the influence of substrate material porous structure on intrinsic activity of catalyst materials. The samples were labeled as ATP200/CeO_2/Soot, ATP325/CeO_2/Soot, Cord200/CeO_2/Soot and Cord 325/CeO_2/Soot.

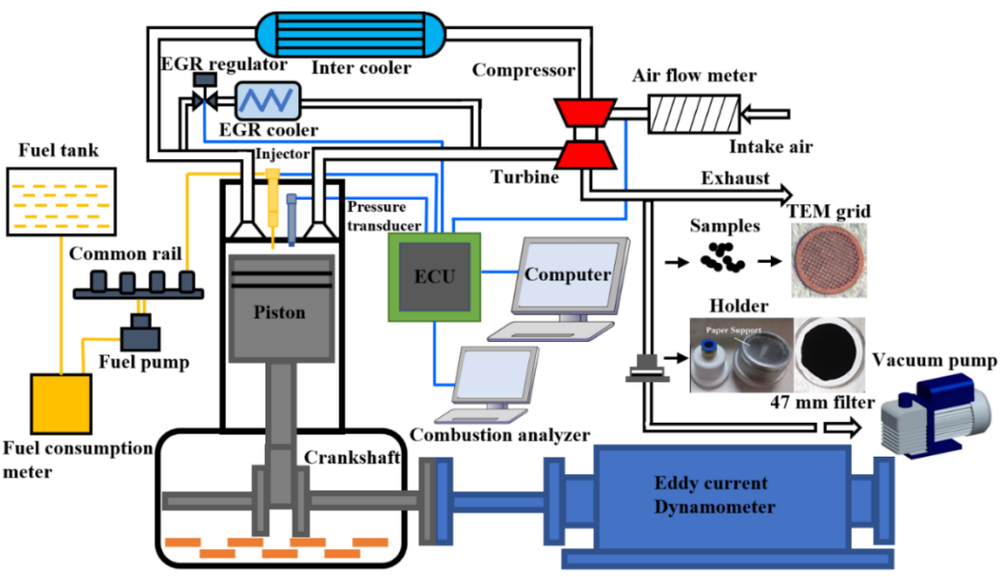

158 **Fig. 2.** Schematic diagram of the engine set-up and sampling system

159 **Table 1** Engine specifications

Categories	Properties
Number of cylinders	4
Max speed	2800 r/min
Stroke	118 mm
Bore	102 mm
Compression ratio	17:1
Valves per cylinder	4
Displacement	3.865 L
Fuel injection system	Common rail direct injection

160 **2.2 Characterization methods**

161 The morphological characteristics analyzed in this study mainly include
162 morphology, surface structure, crystalline structure and graphitization degree. The
163 morphology was characterized by scanning electron microscopy (SEM, Hitachi
164 Regulus 8100, Japan), coupled with energy dispersive spectroscopy (EDS, INCA-350,
165 Oxford, UK). EDS was employed to examine the elemental distribution on sample
166 surface. The surface area and total pore volume were determined through N_2
167 physisorption under -196 °C using Micromeritics TriStar II 3030 (USA), in accordance
168 with the Brunauer-Emmett-Teller (BET) method for physical adsorption, as well as the
169 Barrett-Joyner-Halenda (BJH) method for pore diameter. The crystalline structure of
170 sample was analyzed using X-ray diffraction (XRD, Bruker AXS D8-Focus, Germany).
171 Standard Cu/Kα radiation (λ = 0.154 nm) was utilized at 40 kV and 40 mA, covering a
172 scanning range of 3º to 90º. The standard compounds reported in the JCPDS database
173 were employed to identify the diffraction peaks corresponding to the crystalline phases,
174 which primarily facilitated the identification of mineral phases. Qualitative analysis
175 was performed by the MDI Jade 6.0 computer program.

Table 2 The TGA specific heat-up program

Stages	Descriptions
0	Samples in nitrogen
1	Initial temperature 25 ℃
2	Ramp 10 ℃/min to 450 ℃
3	Isothermal for 30 min
4	Air introduced
5	Ramp 2.5 ℃/min to 650 ℃

The soot graphitization degree was assessed by Raman analysis. The first-order original spectrum of the substrate/catalyst sample was obtained through Raman spectrometer with a wavelength of 514.5 nm and source power of 9.3 μW. The low-pressure atomic line lamp was used to calibrate the spectral resolution of the Raman spectrometer. The soot oxidation rate was analyzed using ZCT-A Simultaneous Thermal Analyzer. The thermal treatment is listed in Table 2. The volatile organic fraction, which was mainly consisted of organic carbon, could be removed by thermal treatment [58,59]. To remove organic carbon, the soot particle sample was heated to 450 °C and then maintained for 30 min, utilizing high-purity nitrogen as protective gas. During the oxidation stage, air was introduced as oxidizing gas with the temperature increasing from 450 to 650 °C, ensuring complete oxidation during the regeneration process [60]. Additionally, partially oxidized soot samples with a conversion rate of 50% were obtained for further characterization, which were named as ATP200/CeO_2/Soot-oxidized 50%, Cord200/CeO_2/Soot-oxidized 50%, ATP325/CeO_2/Soot-oxidized 50% and Cord325/CeO_2/Soot-oxidized 50%. All results were expected to provide information about the morphological characteristics of Cord and ATP during the

193 thermal oxidation.

194 **3. Results and discussion**

195 **3.1 Characterization of substrate/catalyst**

196 To better understand the changes of morphology and nanostructure during
197 oxidation thermal, the morphology and elemental composition of ATP/Cord doped over
198 CeO_2 were analyzed by SEM-EDS. The Fig. 3 illustrates the typical images of
199 ATP200/CeO_2, ATP325/CeO_2, Cord200/CeO_2 and Cord 325/CeO_2 without thermal
200 treatment. High magnification images were employed to analyze morphological
201 relationship between substrate and soot, revealing significant differences in texture, size
202 and dispersion. All samples exhibited numerous typical fibers approximately 0.5 to 2
203 μm in length, arranged into bundles. The morphology of ATP clay confirmed the
204 fibrous or rod-like structure. The whisker-like surface was believed to enhance soot
205 particle filter. On the other hand, the Cord displayed a block-like structure with some
206 clumps and smooth surfaces, which was associated with its slipperiness. The
207 morphology of Cord showed varying degrees of micro-cracking.

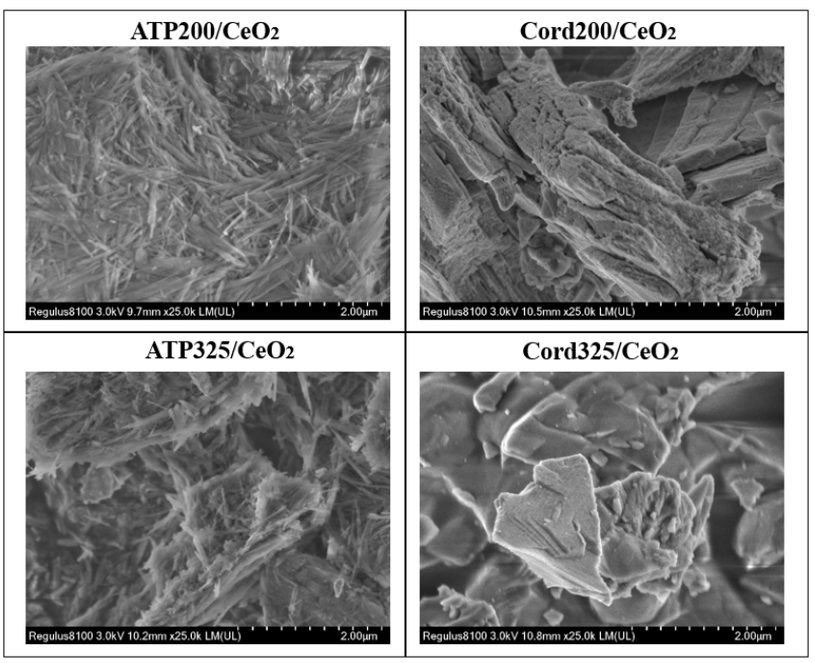

208
209 **Fig. 3.** SEM images for substrate/catalyst samples.

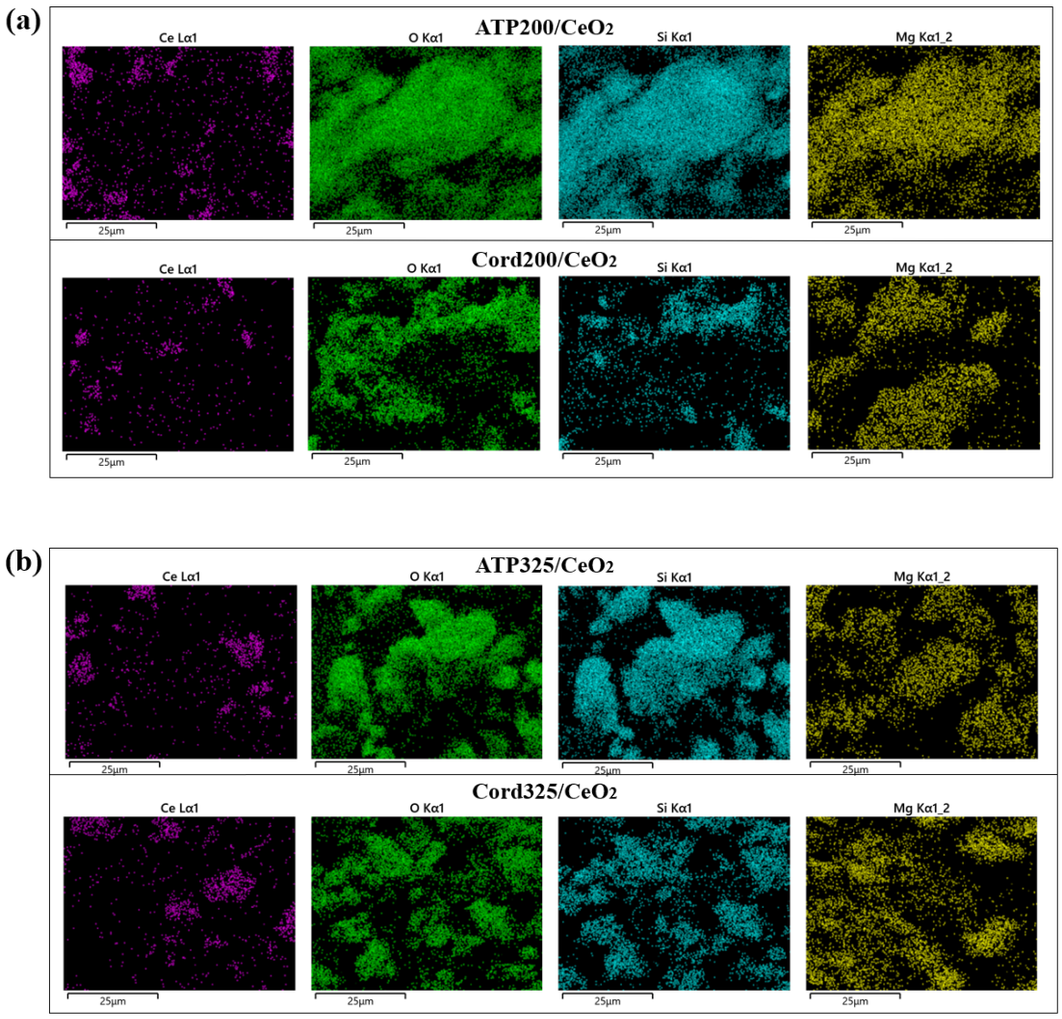

Fig. 4. Elemental mapping for catalyst/substrate samples.

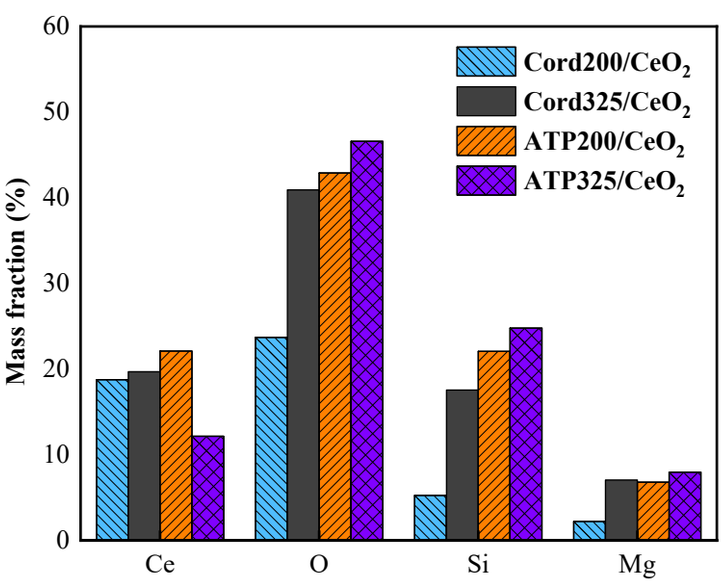

Fig. 5. The elemental mass fraction in catalyst/substrate samples.

To identify and trace the clay and catalyst elements in the ATP/Cord, EDX mappings were conducted for each sample. The Fig. 4 shows the elemental analysis results of ATP200/CeO_2, ATP325/CeO_2, Cord200/CeO_2 and Cord 325/CeO_2. The mass fractions of Ce, O, Si and Mg are listed in Fig. 5. The Ce (pink) was totally from CeO_2 catalyst which was tightly contacted with ATP/Cord by grinding method. The electron probe moved over the surface in raster fashion, and a map of surface composition was conducted. The EDS could reveal the element distribution and concentration on the sample surface. The fibrous or rod-like structure of ATP produced higher surface area and pore volume, which promote the CeO_2 to enter the pores. However, due to the block-like structure of Cord, the catalyst particles mainly distributed on Cord surface. Therefore, the Cord might display higher relative content of Ce in EDS mapping. The distribution of cerium was more compact and uniformly shaped, indicating higher concentration and intensity. The CeO_2 coated on substrate external surface demonstrated a better catalytic performance. The Si (blue) and Mg (yellow) signals were generated by compositions presented in Cord and ATP substrates. As anticipated, Si (blue) and O (green) elements were two dominant in ATP/Cord, which shared the same spots in EDS mapping. For ATP and Cord silicate minerals, there were similar distribution for these four elements. The O was the most abundant element for all samples. It was clearly that the relative content of Ce element in Cord was bigger than it in ATP due to smaller molecular mass of Cord material.

3.2 Thermal oxidation behavior

To analyze the change of morphology and nanostructure of ATP and Cord during thermal treatment, the oxidation tests from 450 to 650 ℃ were conducted on TGA. The normalized mass loss versus temperature curves of ATP200/CeO_2/Soot, Cord200/CeO_2/Soot, ATP325/CeO_2/Soot and Cord325/CeO_2/Soot are presented in Fig.

6. Comparing with Cord, the ATP resulted in notable leftward shift of mass loss curves, indicating an enhancement on soot oxidation. The oxidation behavior of diesel soot was also tested. Obviously, the Cord or ATP mixed with CeO_2 showed higher soot oxidation reactivity than diesel soot.

The temperatures defined as T10, T50, and T90 corresponded to soot samples with 10%, 50%, and 90% mass loss, respectively. Lower characteristic temperature indicated that higher oxidation rate [61,62]. As shown in Table 3, when the Cord was replaced by ATP, the T10, T50, and T90 for 200 mesh samples decreased by 15.9 °C, 13.7 °C and 13.1 °C, respectively. For 325 mesh samples, the T10, T50 and T90 decreased by 6.6 °C, 15.3 °C and 11.2 °C, respectively. In addition, to quantitatively evaluate the oxidation reactivity of soot samples, activation energy (*Ea*) was derived from TGA curve through the Arrhenius model in Eq. (1).

$$-dm/dt = A \cdot exp(-Ea/RT) \cdot m^n \cdot P^r \quad (1)$$

where t is the reaction time; m is the instantaneous mass of soot sample; A is the preexponential factor; Ea is the activation energy; R is gas constant; T is the reaction temperature of soot sample; n is reaction order, which is considered as 1; P and r are partial pressure and reaction order of oxygen, respectively. The reaction order of oxygen is determined to be 1 by referring to the previous studies [63-65]. Eq. (1) can be rearranged as:

$$ln(-dm/mdt) = ln(AP) - Ea/RT \quad (2)$$

where the oxidation kinetic parameters, Ea and A, are estimated from the slope and intercept of $ln(-dm/mdt)$ against $1/T$, respectively. The calculations of soot-

oxidation kinetic analysis were shown in Fig. 7. As shown in Table 3, for ATP200/CeO_2/Soot, the *Ea* value is 138.6 kJ/mol, and 152.6 kJ/mol for the Cord200/CeO_2/Soot, 134.4 kJ/mol for the ATP325/CeO_2/Soot, 144.5 kJ/mol for the Cord325/CeO_2/Soot. The *Ea* value of diesel soot is 178.9 kJ/mol, indicating that the lowest soot oxidation reactivity. It can be seen the *Ea* with the order: ATP < Cord. Higher *Ea* indicated lower oxidation reactivity, indicating more resistance towards oxidation. The soot oxidation mechanism primarily depended on the reactive oxygen species at catalyst-soot contact points. The CeO_2 coated on ATP produced rich array of active oxygen catalytic sites, along with sufficient reaction surface area. In addition, the well-dispersed nanostructure of ATP produced more contact points between CeO_2 and oxygen, allowing it to reversibly exchange oxygen through oxidation reaction.

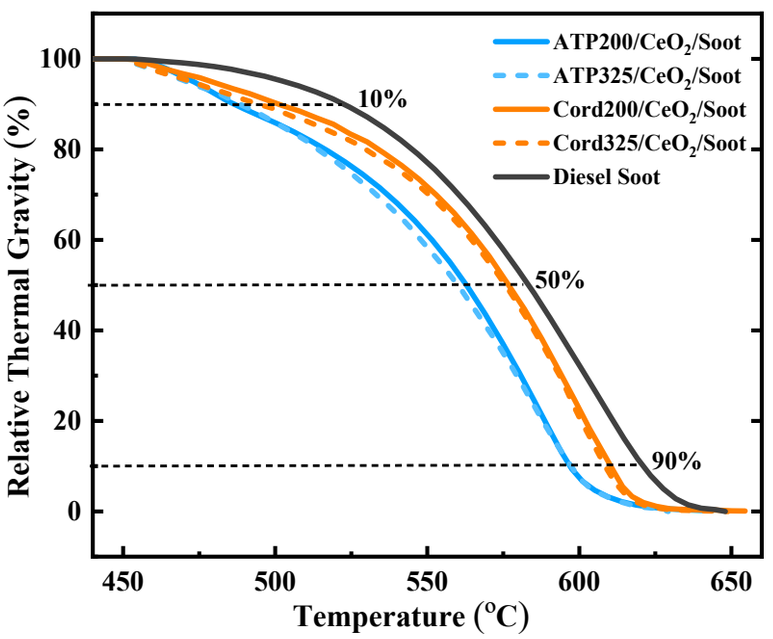

Fig. 6. Thermogravimetric analysis for soot samples.

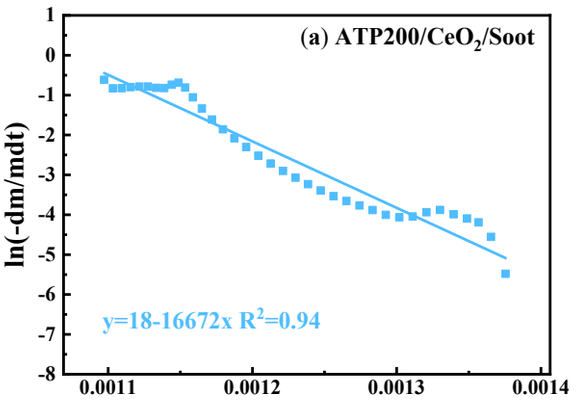

275

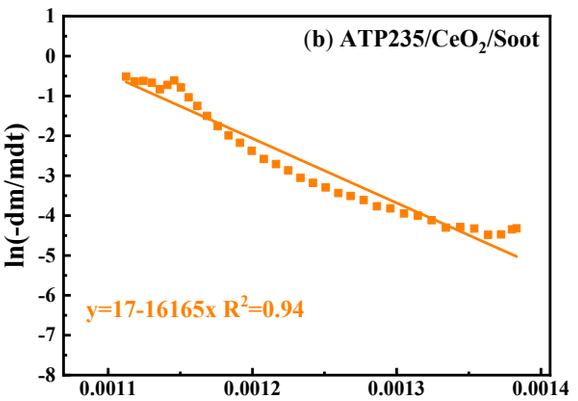

276

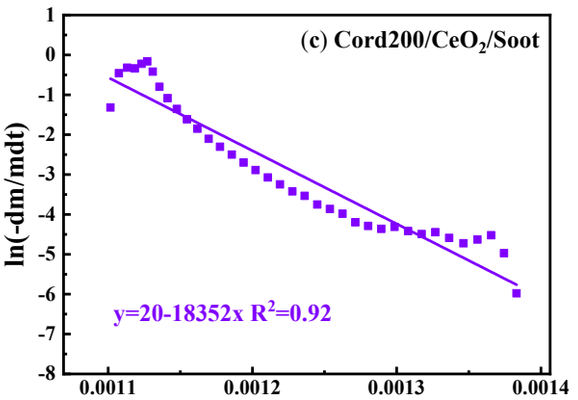

277

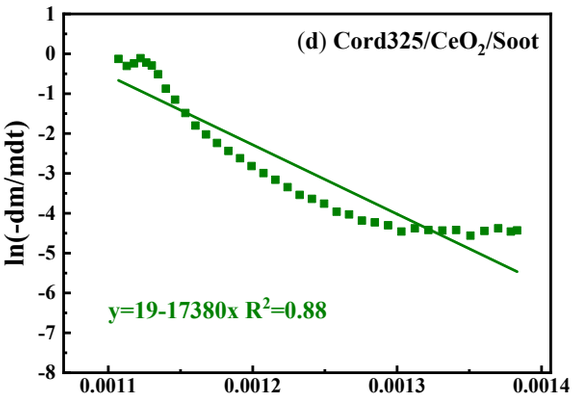

278

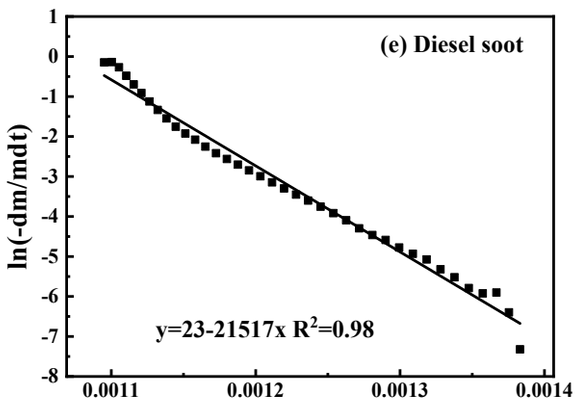

279

280 **Fig. 7.** Soot-oxidation kinetic analysis based on an Arrhenius mode.

281 **Table 3** Oxidation characteristic temperature and activation energy (*Ea*)

Samples	T10 ℃	T50 ℃	T90 ℃	*Ea* (kJ/mol)
Cord200/CeO_2/Soot	501.6	576.6	609.8	152.6
Cord325/CeO_2/Soot	495.2	575.7	608.8	144.5
ATP200/CeO_2/Soot	485.7	562.9	596.7	138.6
ATP325/CeO_2/Soot	488.6	560.4	597.6	134.4
Diesel Soot	522.9	583.7	620.5	178.9

282

283 **3.3 Morphology changes during thermal oxidation**

284 *3.3.1 SEM morphology*

285 Shorter distance and more contact points between soot and catalyst represented
286 better catalytic performance of substrate porous material [66]. Consequently, it was
287 essential to investigate the morphology changes of ATP and Cord during thermal
288 oxidation process. The Fig. 8 shows typical SEM images of ATP200/CeO_2/Soot,
289 Cord200/CeO_2/Soot, ATP325/CeO_2/Soot and Cord325/CeO_2/Soot under different
290 oxidation degrees (0%, 50% and 100%).

291 In Fig. 8 (a) and (c), the enlarged images revealed that ATP was primarily
292 consisted of irregularly arranged rod-shaped structures. The yellow dotted lines were

293 employed to completely circle the diesel soot particles in SEM images. The dispersed
294 soot particle aggregates were uniformly distributed within the ATP, ranging from 0.4-
295 1.2 μm. A careful observation showed an important finding that most soot particle were
296 captured by the rod-like structure of ATP, which was favorable with the contact
297 between soot, CeO_2 and oxygen. At oxidation degree of 50%, ATP whiskers became
298 fewer in number and more scattered. Along with thermal oxidation, the diameter of soot
299 particle aggregate decreased to 0.2-0.6 μm. After thermal treatment, the morphology of
300 ATP was back to before its thermal oxidized, indicating better consistency of catalytic
301 performance. The change of fibrous or rod-like structure could be ignored. As shown
302 in Fig. 8 (b) and (d), the soot particles on Cord displayed uniform and dense distribution.
303 Obviously, along with thermal oxidation, the dense soot particle distribution gradually
304 decreased obviously. Before oxidation, the diameter of soot particle aggregate was
305 above 3 μm, completely covered by substrate material. At oxidation degree of 50%, the
306 surface soot particles were oxidized, the aggregate size decreased at least 1 μm.
307 Comparing with ATP, the block-like structure of Cord only acted as a substrate, and
308 did not promote the contact between soot, oxygen and CeO_2 catalyst.

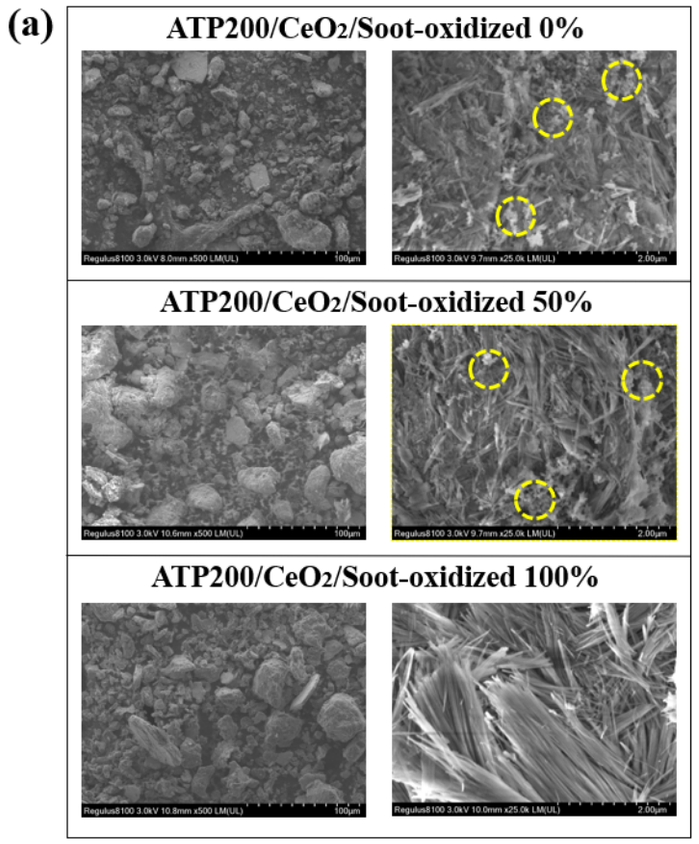
(a)
ATP200/CeO2/Soot-oxidized 0%
ATP200/CeO2/Soot-oxidized 50%
ATP200/CeO2/Soot-oxidized 100%

309

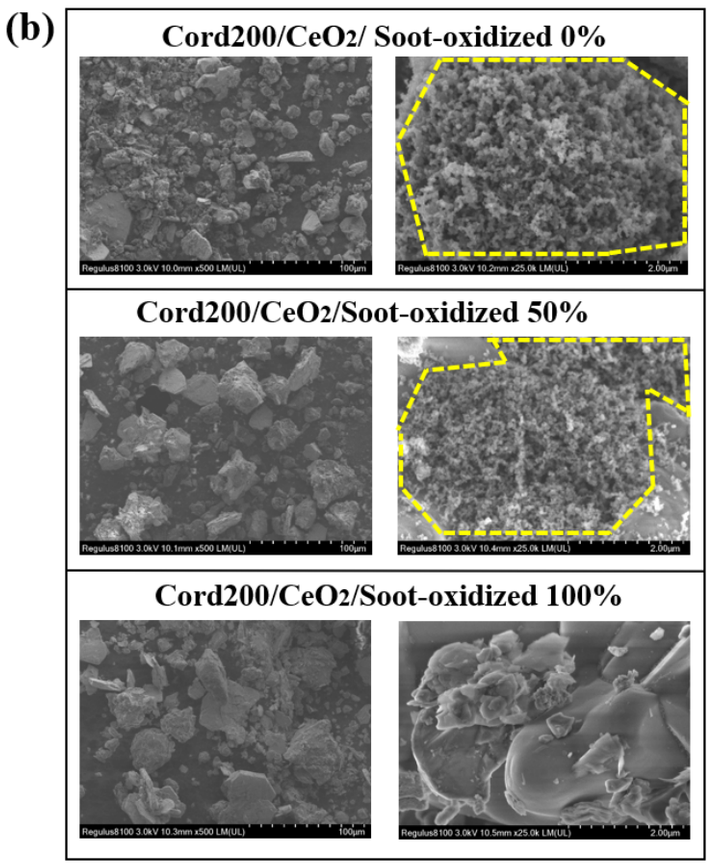
(b)
Cord200/CeO2/ Soot-oxidized 0%
Cord200/CeO2/Soot-oxidized 50%
Cord200/CeO2/Soot-oxidized 100%

310

(c)

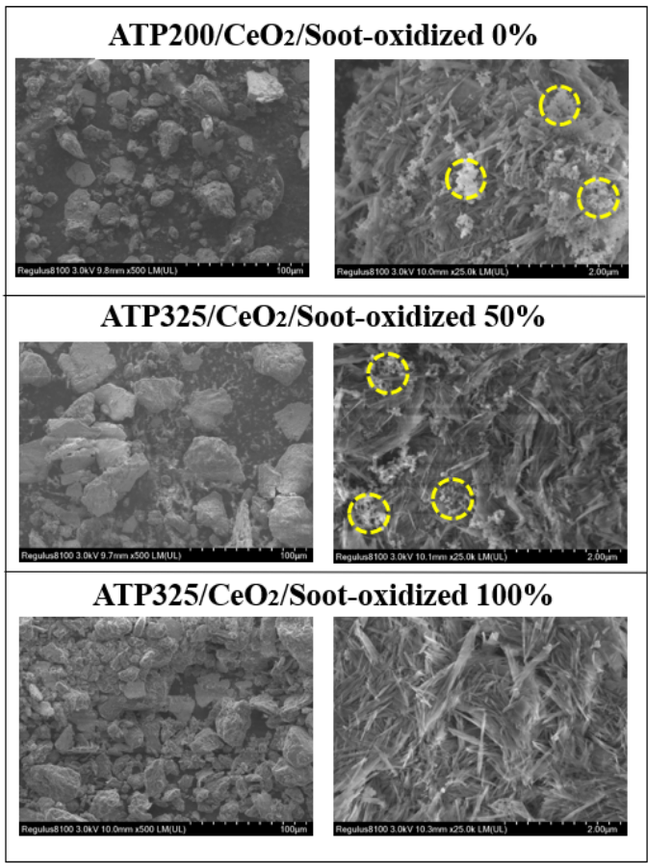
ATP200/CeO2/Soot-oxidized 0%
ATP325/CeO2/Soot-oxidized 50%
ATP325/CeO2/Soot-oxidized 100%

311

(d)

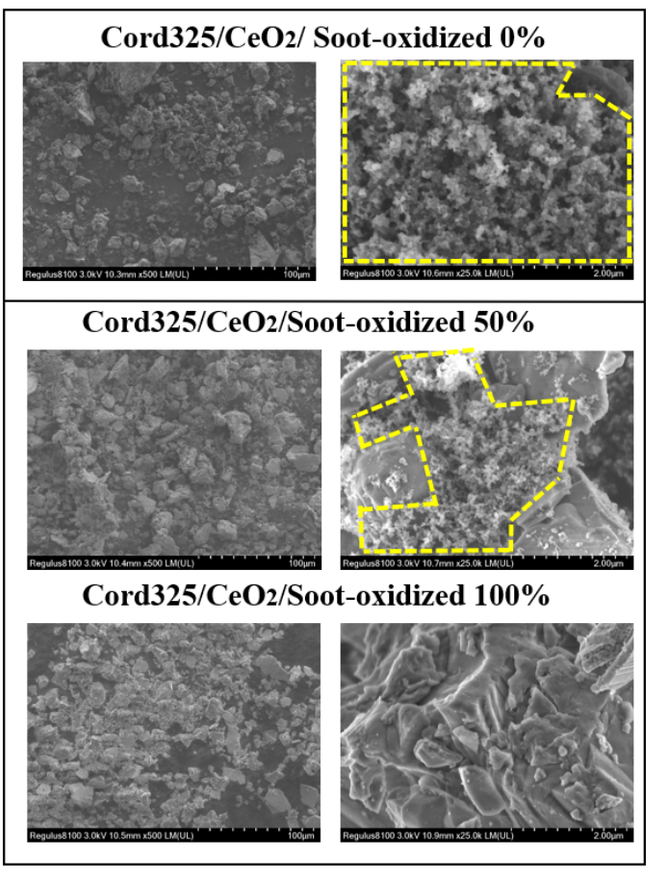
Cord325/CeO2/ Soot-oxidized 0%
Cord325/CeO2/Soot-oxidized 50%
Cord325/CeO2/Soot-oxidized 100%

312

313 **Fig. 8.** SEM morphology for substrate/ catalyst samples

314 *3.3.2 Surface structure*

315 To better understand the correlation between surface structure and catalytic
316 performance, the surface structures of ATP200/CeO_2/Soot, Cord200/CeO_2/Soot,
317 ATP325/CeO_2/Soot and Cord325/CeO_2/Soot were analyzed by BET. As shown in Fig.
318 9, the surface area and total pore volume of ATP are significantly larger than Cord
319 before and after oxidation, respectively. The special fibrous or rod-like structure of ATP
320 produced more pores with the increase of surface area. The block-like structure of Cord
321 had a relatively poor pore-forming capacity. Along with thermal oxidation, for each of
322 sample, the pore diameter increased, but pore volume decreased. The clay mesh number
323 had no obvious effect on pore volume. The pore volume and surface area decreased
324 which was caused by the thermal sintering.

325 There was a clear correlation between soot thermal oxidation temperature and
326 specific surface area. The soot oxidation temperature of substrate/catalyst sample
327 decreased with increased surface area and pore volume, which were beneficial for
328 catalytic oxidation performance. Higher surface area increased the number of active
329 catalytic site, thereby enhancing the soot oxidation reaction. The CeO_2 catalyst
330 generated more active sites, oxygen species and a stronger dispersion of active
331 components by large surface area of ATP, which improved the residence time and
332 deposition rate of soot particle. The interaction between soot particle, active site and
333 active oxygen species was enhanced by the increased surface area, resulting in higher
334 oxidation activity. Consequently, a fine and uniform distribution of CeO_2 was achieved
335 due to the large specific surface area and smaller pore size. These results well explained
336 why soot particles coated on ATP had better oxidation reactivity.

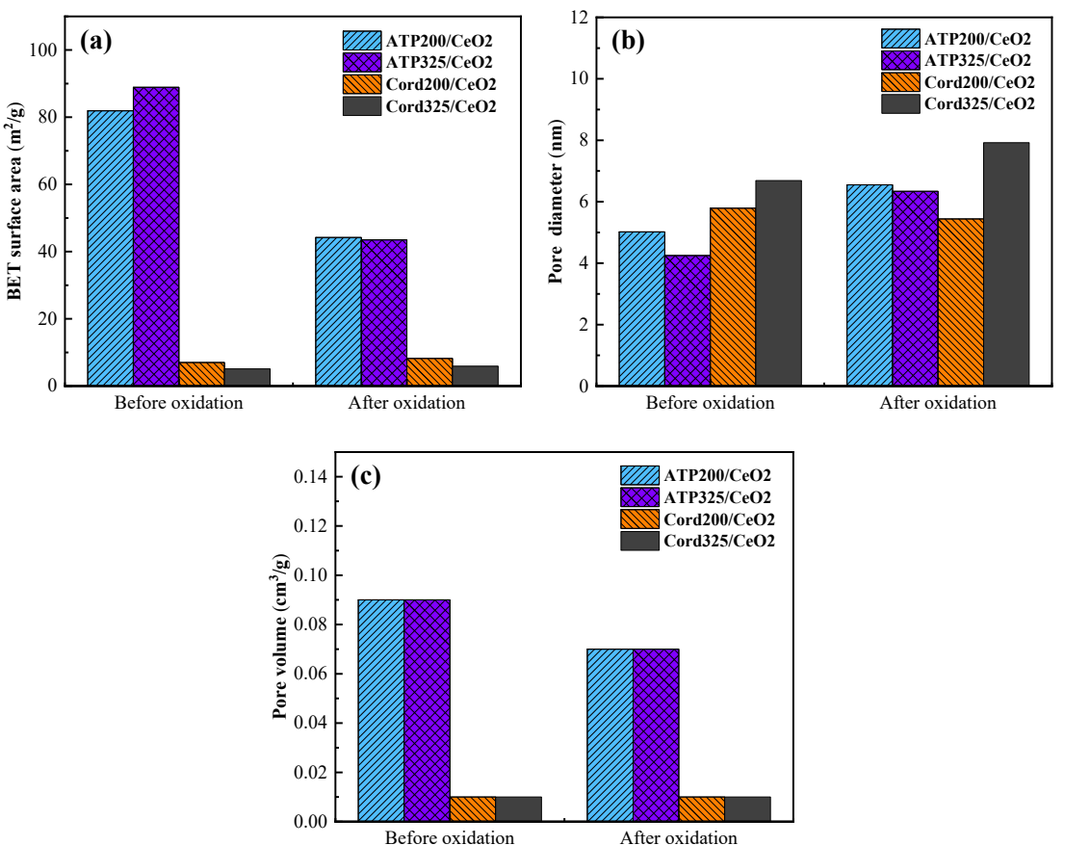

Fig. 9. Surface structure of substrate/catalyst samples before and after oxidation: (a) Surface are, (b) Pore diameter and (c) Pore volume.

3.3.3 Crystalline structure

In order to analyze the impact of thermal oxidation on ATP and Cord structures, quantitative crystalline information was obtained by XRD. The XRD patterns of substrate/catalyst samples under oxidation degrees of 0% and 50% are depicted in Fig. 10. The characteristic peak positions observed at 8.5°, 19.9° and 26.6° correspond to the (110), (040) and (400) planes of ATP clay, respectively [67]. Due to the high degree of ATP crystallinity, the most intense peak was located at 26.6°. The diffraction peak observed at 8.5° was attributed to the basal spacing of ATP framework. The peak at 8.5° nearly disappeared after 50% partial oxidation, as evidenced by its markedly low

intensity. The diffraction peak at near 8.5° was a characteristic peak of ATP, which is different from other minerals. The (110) diffraction peak of ATP at 8.31° weakened after hydrothermal reaction with a more obvious decreasing of peak intensity, resulting from the partial collapse of the crystal framework [68]. The decreased intensity of ATP diffraction peak at 8.4° derived from the increase of calcination temperature. Therefore, this reduction was attributed to the decrease of the basal distance between interlayers of ATP by thermal oxidation. Diffraction peaks at 28.5°, 33.0°, 47.5° and 56.4° corresponded to the (111), (200), (220), and (311) planes of CeO_2, respectively. These peaks exhibited a cubic fluorite structure, in accordance with the standard JCPDS card number 34-0394 [69]. During the thermal oxidation, the XRD pattern of CeO_2 showed no significant changes, indicating the stability of the ATP/CeO_2 catalytic performance.

As illustrated in Fig. 10 (b), peaks located at 10.5°, 21.8°, and 26.4° are associated with (110), (112) and (132) planes of Cord clay, respectively, based on JCPDS card number 12-0303 [70]. The characteristic peaks of Cord remained unchanged before and after thermal oxidation, confirming the structural integrity of its crystalline framework. The block-like structure of Cord was not affected by thermal oxidation reaction. Notably, the CeO_2 exhibited the highest lattice strain, which correlated with its elevated catalytic activity. The intensity of the CeO_2 diffraction peaks corresponding to (200) and (311) slightly decreased after thermal treatment. When CeO_2 was doped onto Cord, the particle size and crystal structure of CeO_2 were influenced by thermal oxidation.

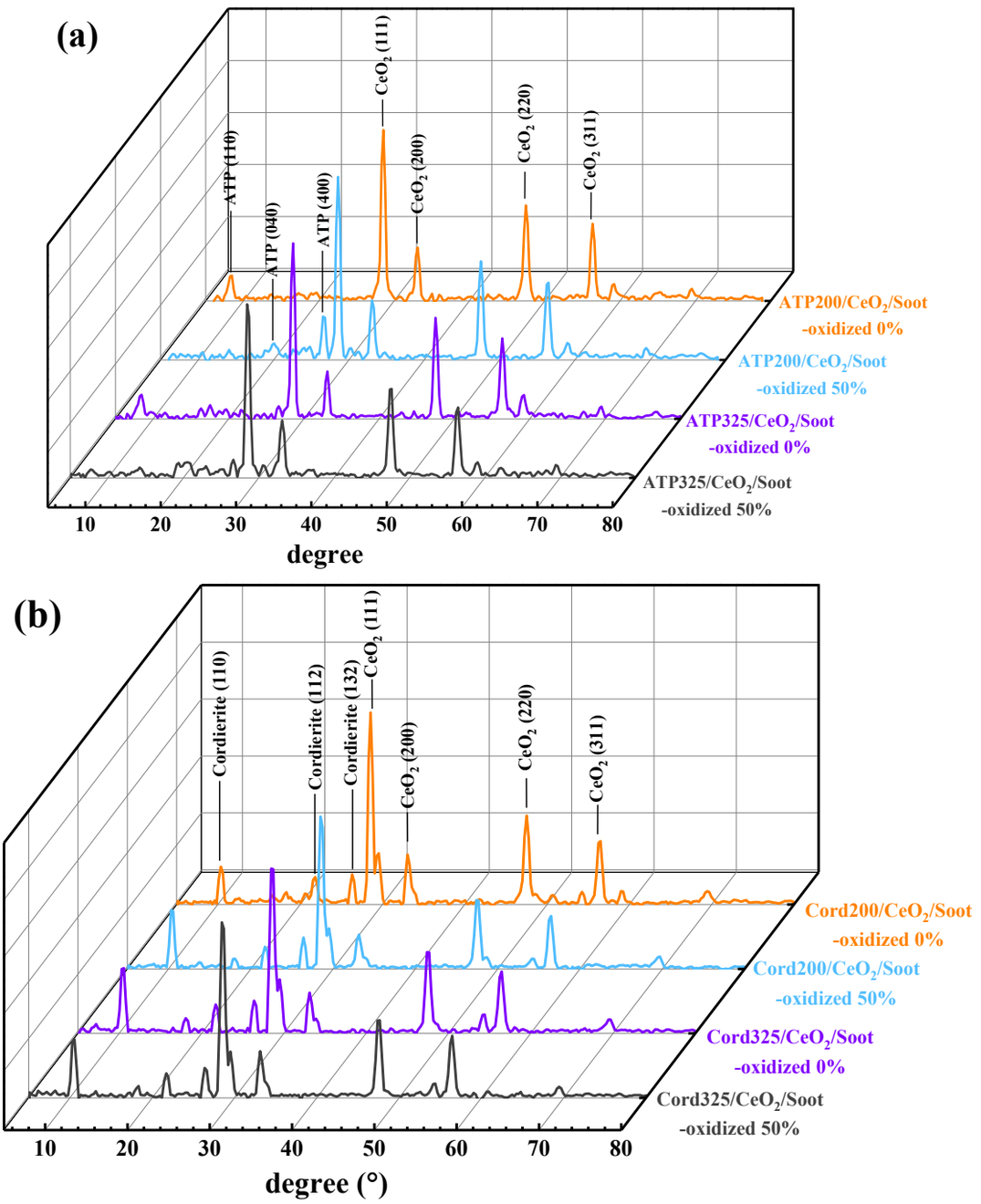

Fig. 10. XRD patterns of substrate/catalyst samples under 0% and 50% oxidation degrees: (a) ATP and (b) Cord.

3.3.4 Graphitization degree

To supplement the nanostructure information of substrate/catalyst samples, the graphitization degree was assessed by Raman analysis. As illustrated in Fig. 11, the 3L1G method is employed for Raman spectrum curves fitting, which includes three

Lorentzian bands at approximately 1590 cm^{-1} (G band), 1360 cm^{-1} (D1 band) and 1200 cm^{-1} (D4 band), along with a Gaussian band near 1500 cm^{-1}. The peak intensity of G band corresponds to the in-plane bond stretching vibrations of ideal graphite, whereas the D band is related to lower or minimal symmetry in hexagonally structured crystals [71]. The relative ratios of D1 and G band areas (A_{D1}/A_G) are presented in Table 4, with standard errors derived from three repeated tests. Some researchers have demonstrated that a lower A_{D1}/A_G ratio represented higher graphitization degree of sample nanostructure [72,73].

With a conversion rate of 50%, all of the A_{D1}/A_G values significantly decreased, indicating the increase of soot graphitization degree. During thermal oxidation, the number of graphite carbon layer increased with typical shell/core shape, consisting of inner-core region and outer shell formed by well-ordered carbon layer [60]. The certain functional groups between the carbon layers were removed, resulting in a more ordered graphitic lattice structure [74]. In this study, the difference of A_{D1}/A_G between 0% and 50% oxidation degrees represented the soot aging degree. Notably, the A_{D1}/A_G difference of ATP sample was bigger than that of Cord. This indicated that the CeO_2 coated on ATP had better catalytic performance because of higher oxygen capacity and more active sites. This results also verified the thermal oxidation behavior in Section 3.2.

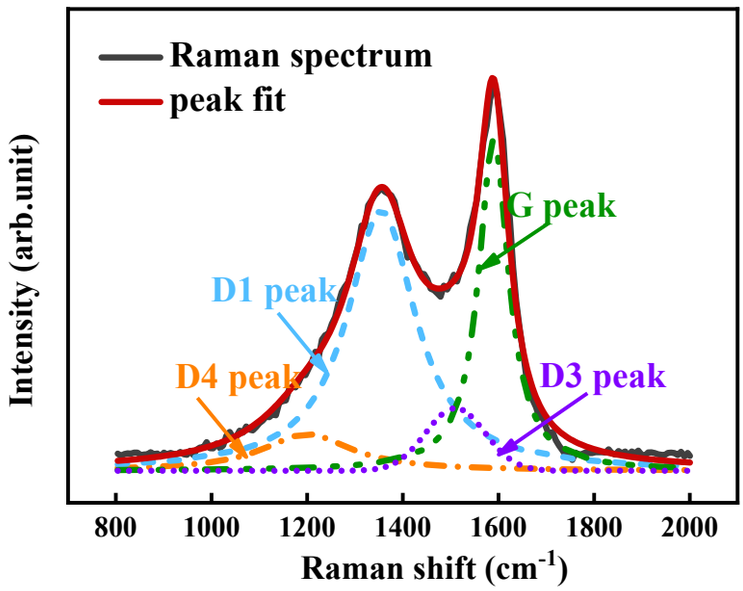

Fig. 11. Raman spectrum analysis and curve fit.

Table 4 Ratios of A_{D1}/A_G for samples

Samples	A_{D1}/A_G	Std.
ATP200/CeO_2/Soot-oxidized 0%	2.76	0.1
Cord200/CeO_2/Soot-oxidized 0%	2.43	0.01
ATP325/CeO_2/Soot-oxidized 0%	2.46	0.09
Cord325/CeO_2/Soot-oxidized 0%	2.5	0.04
ATP200/CeO_2/Soot-oxidized 50%	2.22	0.03
Cord200/CeO_2/Soot-oxidized 50%	2.33	0.01
ATP325/CeO_2/Soot-oxidized 50%	2.08	0.04
Cord325/CeO2 /Soot-oxidized 50%	2.36	0.03

Based on the above analysis of morphology characteristics, there was an efficient heat recovery mechanism after thermal oxidation for ATP. The SEM analysis of ATP revealed minor changes in the material's morphology microstructure. Before and after thermal oxidation, the irregularly arranged rod-shaped structures were always presented in ATP whiskers. Similarly, the block-like structure of Cord only acted as a substrate. The effect of thermal oxidation on the block-like structure of Cord could almost be

406 ignored. The XRD peak intensities of ATP characteristic peaks corresponding to (040)
407 and (400) planes and Cord characteristic peaks corresponding to (110), (112) and (132)
408 showed no changes after oxidized 50%, indicating better stability of crystalline
409 structure. Meanwhile, the peak intensities of CeO_2 characteristic peaks had no changes
410 before and after oxidation. To better evaluate the cyclic stability of substrate materials,
411 the BET analysis was performed before and after thermal oxidation. The change rates
412 of pore volume and pore diameter of Cord before and after thermal oxidation are less
413 than 15%. Although the surface area of ATP decreased from 81.9 to 44.2 m^2/g, it is also
414 significantly bigger than that of Cord. Therefore, in present study, both substrate
415 materials of catalyst demonstrated superior stability.

416 In summary, the position relationship between soot particle, oxygen and CeO_2
417 catalyst within the ATP and Cord substrates are illustrated in Fig. 12. The morphology
418 characteristics were critical factors in terms of catalytic performance. Comparing with
419 block-like structure of Cord, the fibrous or rod-like structure of ATP produced higher
420 surface area and pore volume, which could capture more soot particles because of its
421 higher specific surface area, pore volume, as well as higher capacity of CeO_2 catalyst
422 and oxygen molecules. On the other hand, the distances between soot, catalyst and
423 oxygen played a crucial role in catalytic reaction, which decreased by the fibrous or
424 rod-like structures of ATP, as well as higher catalytic activity. The fibrous morphology
425 was the best one for passive regeneration, which promoted solid–solid interaction. The
426 morphology of ATP showed special fibrous or rod-like structure. The solid–solid
427 interactions between CeO_2 catalyst and soot particles were enhanced by fibrous or rod-

like structure of ATP, indicating more complete catalytic reaction.

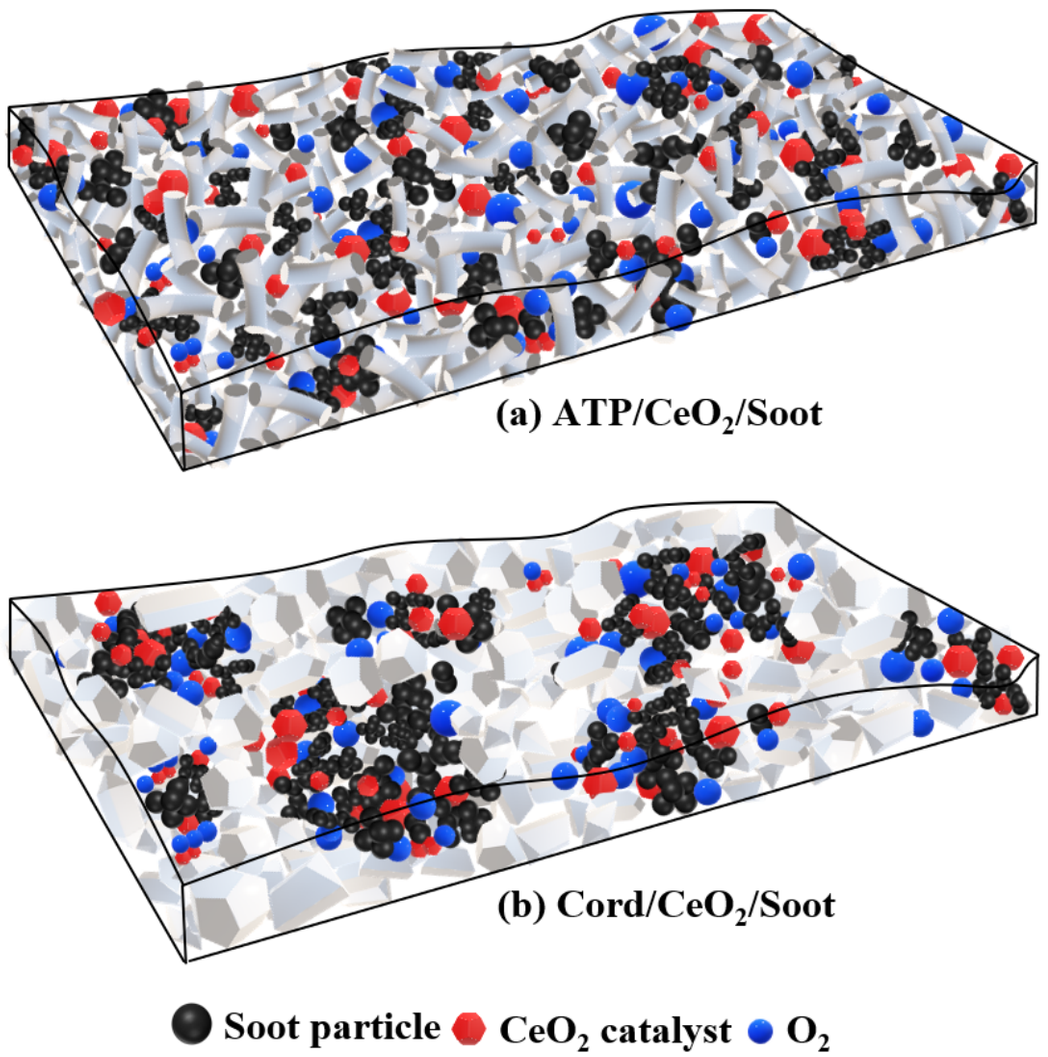

Fig. 12. Schematics of oxygen-soot-catalyst contact condition in different catalyst substrates of (a) ATP and (b) Cord

4. Conclusion

Based on thermal oxidation test, the morphological characteristics of ATP and Cord were measured. The main conclusions are as follows:

(1) The special fibrous or rod-like structure of ATP produced more pore volume and surface area. There was a heat recovery mechanism that the morphology of ATP

was back to what it was before thermal oxidation, indicating favorable consistency of catalytic performance. However, the basal spacing of ATP framework was reduced by thermal oxidation.

(2) Increasing the oxidation conversion led to the decrease of uniform and dense distribution of soot particle on Cord surface. The block-like structure of Cord only acted as a substrate, and does not promote the contact between soot, oxygen and CeO_2 catalyst. The XRD diffraction peak of Cord exhibited no changes before and after thermal oxidation, which confirmed that the crystalline structure of Cord remained intact during thermal oxidation.

(3) The ATP provided more active sites of catalyst and sufficient reaction surface area for the soot-O_2-CeO_2 reaction, resulting in higher soot graphitization degree. The oxidation reactivity of ATP/CeO_2/Soot system was higher than Cord/CeO_2/Soot system, in which a certain decrease of activation energy and characteristic oxidation temperatures.

The future research should focus on the comparison of structural stability and particulate filter efficiency between ATP and Cord. The difference of soot oxidation behavior between ATP and Cord in real DPF channels will be investigated.

Declaration of interest statement

The authors declare that they have no known competing financial interests or personal relationships that could have appeared to influence the work reported in this paper.

Acknowledgments

This work was supported by Key Research and Development Program of Gansu

Province (25YFWA015) and the Science and Technology Planning Project of Gansu Province (24CXGA049).

References

[1] J. Fang, Z. Meng, J. Li, Y. Du, Y. Qin, Y. Jiang, W. Bai, G.G. Chase, The effect of operating parameters on regeneration characteristics and particulate emission characteristics of diesel particulate filters, Appl. Therm. Eng. 148 (2019) 860-867. https://doi.org/10.1016/j.applthermaleng.2018.11066.

[2] Y. Shi, Y. Cai, R. Fan, Y. Cui, Y. Chen, L. Ji, Characterization of soot inside a diesel particulate filter during a nonthermal plasma promoted regeneration step, Appl. Therm. Eng. 150 (2019) 612–619.

[3] L. Lisi, G. Landi, V. Di Sarli, The Issue of Soot-Catalyst Contact in Regeneration of Catalytic Diesel Particulate Filters: A Critical Review, Catalysts. 10 (2020) 1307.

[4] Y.W. Deng, W.P. Zheng, J.Q. E, B. Zhang, X.H. Zhao, Q.S. Zuo, Z. Zhang, D.D. Han, Influence of geometric characteristics of a diesel particulate filter on its behavior in equilibrium state, Appl. Therm. Eng. 123 (2017) 61-73.

[5] H. Caliskan, K. Mori, Environmental, enviroeconomic and enhanced thermodynamic analyses of a diesel engine with diesel oxidation catalyst (DOC) and diesel particulate filter (DPF) after treatment systems, Energy. 128 (2017) 128-44.

[6] J. Benajes, A. García, J. Monsalve-Serrano, V. Boronat, An investigation on the particulate number and size distributions over the whole engine map from an optimized combustion strategy combining RCCI and dual-fuel diesel-gasoline, Energy. Convers. Manag. 140 (2017) 98-108.

[7] X. Zhao, J. Jiang, H. Zuo, G. Jia, Soot combustion characteristics of oxygen concentration and regeneration temperature effect on continuous pulsation regeneration in diesel particulate filter for heavy-duty truck, Energy. 264 (2023) 126265.

[8] D. Wang, J. Cao, P. Tan, Z. Wang, W. Li, Z. Liu, J. Wang, Full course evolution characteristics of DPF active regeneration under different inlet HC concentrations, Fuel. 310 (2022) 122452.

[9] M. Yu, D. Luss, V. Balakotaiah, Analysis of flow distribution and heat transfer in a diesel particulate filter, J. Chem. Eng. 226 (24) (2013) 68–78.

[10] J. Fang, Z. Meng, J. Li, Y. Du, Y. Qin, Y. Jiang, W. Bai, G.G. Chase, The effect of operating parameterson regeneration characteristics and particulate emission characteristics of diesel particulate filters, Appl. Therm. Eng. 148 (2019) 860–867.

[11] S.J. Lee, S.J. Jeong, W.S. Kim, Numerical design of the diesel particulate filter for optimum thermal performances during regeneration, Appl. Energy. 86 (7) (2009) 1124–1135.

[12] J.R. Serrano, F.J. Arnau, P. Piqueras, O.G. Afonso, Packed bed of spherical particles approach for pressure drop prediction in wall-flow DPFs (diesel particulate filters) under soot loading conditions, Energy. 58 (2013) 644–654.

[13] Z. Meng, J. Li, J. Fang, J. Tan, Y. Qin, Y. Jiang, Z. Qin, W. Bai, K. Liang, Experimental study on regeneration performance and particle emission characteristics of DPF with different inlet transition sections lengths, Fuel. 262 (2020) 116487.

[14] Z. Meng, C. Chen, J. Li, J. Fang, J. Tan, Y. Qin, Y. Jiang, Z. Qin, W. Bai, K. Liang, Particle emission characteristics of DPF regeneration from DPF regeneration bench and

diesel engine bench measurements, Fuel. 262 (2020) 116589.

[15] P. Tan, L. Dua, E. Li, Z. Hu, D. Lou, Experimental study on the temperature characteristics of a diesel particulate filter during a drop to idle active regeneration process, Appl. Therm. Eng. 178 (2022) 115628.

[16] C.T. Lao, J. Akroyd, N. Eaves, A. Smith, N. Morgan, A. Bhave, M. Kraft, Modelling particle mass and particle number emissions during the active regeneration of diesel particulate filters, Proc. Combust. Inst. 37 (2019) 4831–4838.

[17] K. Laziri, I. Lamara, F.Z. Mezahi, F. Sahnoune, E. Dhahri, S.F. Hassan, N. Saheb, Synthesis, microstructure, hardness, thermal expansion, and dielectric properties of cordierite, Int J Appl Ceram Technol. (2025) e15173.

[18] L.F. Nascimento, J.F. Lima, P.C. de Sousa Filho, O.A. Serra, Control of diesel particulate emission based on Ag/CeOx/FeOy catalysts supported on cordierite, J. Chem. Eng. 290 (2016) 454-464. https://doi.org/ 10.1016/j.cej.2016.01043.

[19] M. Valaskova, K.K. Kupkova, Cordierite/steatite/CeO_2 porous materials: Preparation, structural characterization and their photocatalytic activity, MICROPOR MESOPOR MAT 207 (2015) 120-125. https://doi.org/ 10.1016/j.micromeso.2014.12035.

[20] T. Luo, P. Li, W. Dong, Q. Zeng, X. Yu, X. Gu, G. Dong, Development of cordierite-based low-expansion porcelain tiles with application potential in an underfloor heating system, Int J Appl Ceram Technol. 22 (2025) e15031.

[21] G. Yan, L. Chen, Q. Jiang, L. Zhang, J. Wang, Y. Yang, Z. Li, J. Feng, Thermal/mechanical properties of cordierite synthesized using coal gangue as a

refractory material, Int J Appl Ceram Technol. 22 (2025) e14987.

[22] W. Xu, C. Kou, E. Jiaqiang, C. Feng, Y. Tan, Effect analysis on the flow uniformity and pressure drop characteristics of the rotary diesel particulate filter for heavy-duty truck, Energy. 288 (2024) 129820.

[23] L.F. Nascimento, R.F. Martins, R.F. Silva, O.A. Serra, Catalytic combustion of soot over ceria-zinc mixed oxides catalysts supported onto cordierite, J. Environ. Sci. 26 (2014) 694-701. https://doi.org/ 10.1016/S1001-0742(13)60442-8.

[24] J. Wei, C. Fan, D. Li, Y. Zhuang, Z. Fu, Z. Guan, H. Li, D. Li, Y. Qian, Diesel soot combustion over ceria catalyst: Evolution of functional groups on soot surfaces, Fuel. 338 (2023) 127391. https://doi.org/ 10.1016/j.fuel.2023.127391.

[25] Z. Shi, Y. Liu, W. Yang, K. Liang, F. Pan, S. Gu, Evaluation of cordierite–ceria composite ceramics with oxygen storage capacity, J. Eur. Ceram. Soc. 22 (2002) 1251-1256.

[26] S. Zeng, A. Shui, H. Yu, C. He, Sonochemical synthesis of CeO_2 nanoparticles with high photocatalytic and antibacterial activities under visible light, Int J Appl Ceram Technol. 21 (2024) 3141–3151.

[27] S. Liu, Y. Zeng, D. Jiang, Effects of CeO_2 addition on the properties of cordierite-bonded porous SiC ceramics, J. Eur. Ceram. Soc. 29 (2009) 1795-1802. https://doi.org/ 10.1016/j.jeurceramsoc.2008.11002.

[28] S. Bensaid, N. Russo, D. Fino, CeO_2 catalysts with fibrous morphology for soot oxidation: The importance of the soot–catalyst contact conditions, Catal. Today. 216 (2013) 57–63.

548 [29] M. Zhang, Y. Wang, M. Yu, M. He, L. Cao, X. Luo, W. Wang, Preparation of
549 aluminum borate whiskers/CoxCr3-xO4 catalysts on channel surface of cordierite
550 honeycomb ceramic for soot catalytic combustion, Int J Appl Ceram Technol. 22 (2025)
551 e14994.
552 [30] Y. Liu, C. Su, J. Clerc, A. Harinath, L. Rogoski, Experimental and modeling study
553 of ash impact on DPF backpressure and regeneration behaviors, SAE. Int. J. Engines.
554 8 (3) (2015) 1313–1321.
555 [31] Han Yan, Ningqiang Zhang, Dingsheng Wang, Highly efficient CeO_2-supported
556 noble-metal catalysts: From single atoms to nanoclusters, Chem. Catalysis. 2 (2022)
557 1594–1623.
558 [32] Y. Jin, N. Shinoda, Y. Uesaka, T. Kuki, M. Yamashita, H. Sakamoto, C.D. Vogt,
559 Development of new high porosity diesel particulate filter for integrated
560 SCRtechnology/catalyst, SAE. Int. J. Fuels. Lubr. 8 (2015) 494–500.
561 [33] F. Sandra, A. Ballestero, V.L. Nguyen, M.N. Tsampas, P. Vernoux, C. Balan, Y.J.
562 Iwamoto, U.B. Demirci, P. Miele, S. Bernard, Silicon carbide-based membranes with
563 high soot particle filtration efficiency, durability and catalytic activity for CO/HC
564 oxidation and soot combustion, J. Membr. Sci. 50 (2016) 79-92. https://doi.org/
565 10.1016/j.memsci.2015.12015.
566 [34] M.P. Orihuela, O. Haralampous, R. Chacartegui, M.T. García, J. Martínez-
567 Fernández, Numerical Simulation of a Wall-Flow Particulate Filter Made of
568 Biomorphic Silicon Carbide Able to Fit Different Fuel/Biofuel Inputs, Processes. 7
569 (2019) 945. https://doi.org/ 10.3390/pr7120945.

570 [35] F. Fang, P. Zhao, N. Feng, H. Wan, G. Guan, Surface engineering on porous
571 perovskite-type $La_{0.6}Sr_{0.4}CoO_3$-δ nanotubes for an enhanced performance in diesel soot
572 elimination, J. Hazard. Mater. 399 (2020) 2–12.
573 [36] C. Zhang, D. Yu, C. Peng, L. Wang, X. Yu, Y. Wei, J. Liu, Z. Zhao, Research
574 progress on preparation of 3DOM-based oxide catalysts and their catalytic
575 performances for the combustion of diesel soot particles, Appl. Catal. B. 319 (2022) 2–
576 27.
577 [37] H.J. Guo, Q.L. Li, H.R. Zhang, F. Peng, L. Xiong, S.M. Yao, C. Huang, X.D.
578 Chen, CO_2 hydrogenation over acid-activated Attapulgite/$Ce_{0.75}Zr_{0.25}O_2$
579 nanocomposite supported Cu-ZnO based catalysts, Mol. Catal. 476 (2019) 110499.
580 https://doi.org/ 10.1016/j.mcat.2019.110499.
581 [38] H.J. Guo, H.R. Zhang, F. Peng, H.J. Yang, L. Xiong, C. Huang, C. Wang, X.D.
582 Chen, L.L. Ma, Mixed alcohols synthesis from syngas over activated palygorskite
583 supported Cu-Fe-Co based catalysts, Appl. Clay. Sci. 111 (2015) 83-89. https://doi.org/
584 10.1016/j.clay.2015.03009.
585 [39] J. Cao, G. Shao, Y. Wang, Y. Liu, Z. Yuan, CuO catalysts supported on attapulgite
586 clay for low-temperature CO oxidation, Catal. Commun. 9 (2008) 2555-2559.
587 https://doi.org/ 10.1016/j.catcom.2008.07016.
588 [40] C. Zhu, X. Wang, Q. Huang, L. Huang, J. Xie, C. Qing, T. Chen, Removal of
589 gaseous carbon bisulfide using dielectric barrier discharge plasmas combined with TiO_2
590 coated attapulgite catalyst, J. Chem. Eng. 225 (2013) 567-573. https://doi.org/
591 10.1016/j.cej.2013.03107.

592 [41] X. Li, H. Zhang, H. Lv, S. Zuo, Y. Zhang, C. Yao, Photo-assisted SCR removal of
593 NO by up conversion CeO_2/Pr^{3+}/attapulgite nanocatalyst, Environ. Sci. Pollut. Res. 26
594 (2019) 12842-12850.
595 [42] H. Yan, N. Zhang, D. Wang, Highly efficient CeO_2-supported noblemetal catalysts:
596 From single atoms to nanoclusters. Chem Catalysis 2(7) (2022) 1594-623.
597 [43] X. Deng, M. Li, J. Zhang, X. Hu, J. Zheng, N. Zhang, B. Chen, Constructing nano-
598 structure on silver/ceria-zirconia towards highly active and stable catalyst for soot
599 oxidation, J. Chem. Eng. 313 (2017) 544-555. https://doi.org/ 10.1016/j.cej.2016.12088.
600 [44] Z. Meng, Z. Bao, Z. Chen, B. Zeng, Z. Qin, J. Tan, P. Pu, Experimental effects of
601 ash (ZnO) and catalyst (CeO_2) on DPF regeneration performance and emission
602 characteristics. Fuel 365 (2024) 131193.
603 [45] J. Ou, Z. Meng, Y. Hu, Y. Du, Experimental investigation on the variation
604 characteristics of soot layer thickness and pressure drop during DPF/CDPF active
605 regeneration. Chem. Eng. Sci. 241 (2021) 116682.
606 [46] A. Bueno-López, Diesel soot combustion ceria catalysts, Appl. Catal. B. Environ.
607 146 (2014) 1-11. https://doi.org/ 10.1016/j.apcatb.2015.12030.
608 [47] D. Fino, S. Bensaid, M. Piumetti, N. Russo, A review on the catalytic combustion
609 of soot in diesel particulate filters for automotive applications: From powder catalysts
610 to structured reactors, Appl. Catal. A. Gener. 509 (2016) 75-96. https://doi.org/
611 10.1016/j.apcata.2015.10016.
612 [48] B. Zhao, X. Liang, K. Wang, T. Li, X. Lv, S. Zhang, Impact of sulfur functional
613 groups on physicochemical properties and oxidation reactivity of diesel soot particles,

614 Fuel. 327 (2022) 125041. https://doi.org/ 10.1016/j.fuel.2022.125041.
615 [49] J. Wei, C. Fan, L. Qiu, Y. Qian, C. Wang, Q. Teng, M. Pan, Impact of methanol
616 alternative fuel on oxidation reactivity of soot emissions from a modern CI engine, Fuel.
617 268 (2020) 117352.
618 [50] E. Aneggi, V. Rico-Perez, C. de Leitenburg, S. Maschio, L. Soler, J. Llorca, A.
619 Trovarelli, Ceria-zirconia particles wrapped in a 2D carbon envelope: Improved low-
620 temperature oxygen transfer and oxidation activity. Angew. Chem. Int. Ed. 54 (2015)
621 14040-14043.
622 [51] Y. Wang, J. Wang, H. Chen, M. Yao, Y. Li. Preparation and NOx-assisted soot
623 oxidation activity of a CuO-CeO_2 mixed oxide catalyst. Chemical Engineering Science,
624 135 (2015) 294–300.
625 [52] J. Neeft, M. Makkee, J.A. Moulijn, Catalysts for the oxidation of soot from diesel
626 exhaust gases I An exploratory study, Appl. Catal. B. Environ. 8 (1) (1996) 57-78.
627 [53] X. Liang, Y. Wang, K. Wang, Y. Wang, H. Zhang, B. Zhao, X. Lv, Experimental
628 study of impact of lubricant-derived ash on oxidation reactivity of soot generated in
629 diesel engines, Proc Combust Inst 38(4) (2021) 5635–5642.
630 [54] S. Wagloehner, M. Nitzer-Noski, S. Kureti, Oxidation of soot on manganese oxide
631 catalysts. Chem. Eng. J. 259 (2015) 492–504.
632 [55] T. Andana, M. Piumetti, S. Bensaid, N. Russo, D. Fino, R. Pirone, Nanostructured
633 ceria-praseodymia catalysts for diesel soot combustion, Applied catalyst, Appl. Catal.
634 B. Environ. 197 (2016) 125-137. https://doi.org/ 10.1016/j.apcatb.2015.12030.
635 [56] J. She, T. Ohji, Fabrication and characterization of highly porous mullite ceramics,

636 Mater. Chem. Phys. 80 (2003) 610–614.
637 [57] F. Yang, C. Li, Y. Lin, C.-A. Wang, Effects of sintering temperature on properties
638 of porous Mullite/Corundum ceramics, Mater. Lett. 73 (2012) 36–39.
639 [58] Y. Wang, X. Liang, G. Tang, Y. Chen, L. Dong, G. Shu, Impact of lubricating oil
640 combustion on nanostructure, composition and graphitization of diesel particles, Fuel
641 190 (2017) 237-244.
642 [59] Y. Wang, X. Liang, K. Wang, Y. Wang, L. Dong, G. Shu, Effect of base oil on the
643 nanostructure and oxidation characteristics of diesel particulate matter, Appl. Therm.
644 Eng. 106 (2016) 1311-1318.
645 [60] Y. Liu, X. Zhang, G. Lyu, Y. Qiao, W. Zhang, C. Song, Effect of the oxidation-
646 induced fragmentation of primary particles on soot oxidation reactivity, Combust.
647 Flame. 240 (2022) 112026. https://doi.org/ 10.1016/j.combustflame.2022.112026.
648 [61] X. Liang, Y. Wang, Y. Wang, B. Zhao, Z. Zhang, X. Lv, Z. Wu, X. Cai, K. Wang,
649 Impact of lubricating base oil on diesel soot oxidation reactivity, Combust. Flame. 217
650 (2020) 77-84. https://doi.org/ 10.1016/j.combustflame.2020.03035.
651 [62] Y. Wang, H. Yang, X. Liang, H. Song, Z. Tao, Effect of lubricating base oil on the
652 oxidation behavior of diesel exhaust soot, Sci. Total. Environ. 858 (2023) 160009.
653 https://doi.org/ 10.1016/j.scitotenv.2022.160009.
654 [63] Y. Liu, C.X. Fan, F. Wang, H. Liu, Chen, Thermally induced variations in the
655 nanostructure and reactivity of soot particles emitted from a diesel engine,
656 Chemosphere. 286 (2022) 131712.
657 [64] D. Dollimore, T.A. Evans, Y.F. Lee, F.W. Wilburn, Correlation between the shape

of a TG/DTG curve and the form of the kinetic mechanism which is applying, Thermochim. Acta. 198 (2) (1992) 249–257.

[65] J. Neeft, T.X. Nijhuis, E. Smakman, S. Erik, M. Michiel, J.A. Moulijn, Kinetics of the oxidation of diesel soot, Fuel. 76 (12) (1997) 1129–1136.

[66] V. Palma, P. Ciambelli, E. Meloni, A. Sin, Study of the catalyst load for a microwave susceptible catalytic DPF, Catal. Today. 216 (2013) 185-193. https://doi.org/ 10.1016/j.cattod.2013.07012.

[67] Y.H. Yu, J.C.S. Wu, Removal of NOx by photocatalytic processes, J. Photochem Photobiol. C: Photochem. Rev. 14 (2013) 29-52. https://doi.org/ 10.1016/j.jphotochemrev.2012.08002.

[68] Z. Zhang, W. Wang, Y. Kang, L. Zong, A. Wang, Tailoring the properties of palygorskite by various organic acids via a one-pot hydrothermal process: A comparative study for removal of toxic dyes. Appl. Clay Sci. 120 (2016) 28-39.

[69] Z. Chen, F. Chen, X. Li, X. Lu, C. Ni, X. Zhao, Facile synthesis of CeO_2 nanotubes templated by modified attapulgite, J. Rare. Earths. 28 (4) (2010) 566-570. https://doi.org/ 10.1016/S1002-0721(09)60155-1.

[70] M. Gu, Q. Huang, L. Xu, J. Zhu, Y. Sun, T. Tao, B. Yang, M. Chen, H. Yang, Improved activity and stability for chlorobenzene oxidation over ternary Cu-Mn-O-Ce solid solution supported on cordierite, Environ. Sci. Pollut. Res. 30 (2023) 37535-37546. https://doi.org/ 10.1007/s11356-022-24988-1.

[71] C. Russo, A. Ciajolo, Effect of the flame environment on soot nanostructure inferred by Raman spectroscopy at different excitation wavelengths, Combust. Flame.

680 162 (2015) 2431-2441. https://doi.org/ 10.1016/j.combustflame.2015.02011.
681 [72] Y. Guo, Z. Ristovski, E. Graham, S. Stevanovic, P. Verma, M. Jafari, B. Miljevic,
682 R. Brown, The correlation between diesel soot chemical structure and reactivity,
683 Carbon. 161 (2020) 736-749. https://doi.org/ 10.1016/j.carbon.2020.01061.
684 [73] M. Lapuerta, F. Oliva, J.R. Agudelo, A.L. Boehman, Effect of fuel on thesoot
685 nanostructure and consequences on loading and regeneration of diesel particulate filters,
686 Combust. Flame. 159 (2012) 844-853. https://doi.org/
687 10.1016/j.combustflame.2011.09003.
688 [74] L. Wang, C. Song, J. Song, G. Lv, H. Pang, W. Zhang, Aliphatic C–H and
689 oxygenated surface functional groups of diesel in-cylinder soot: Characterizations and
690 impact on soot oxidation behavior, Proc. Combust. Inst. 34 (2) (2013) 3099–3106.

Impact of thermal oxidation on morphological characteristics of cordierite and attapulgite substrate materials

Bowen Zhao[a]*, Tao Peng[b], Xiaoxue Zhang[b], Junpeng Li[a], Ye Liu[c]*

[a]Lanzhou University of Technology, Lanzhou 730050, China

[b]Gansu Research Institute of Light Industry Co., Ltd., Lanzhou 730099, China

[c]Institute for Transport Studies, University of Leeds, Leeds, LS2 9JT, UK

*Corresponding Authors: zhaobw@lut.edu.cn; Y.Liu8@leeds.ac.uk

Abstract

The diesel particulate filter (DPF) is one of the most effective devices for reducing particulate emission, where the continuous DPF regeneration is necessary for maintaining filter efficiency. There is currently a lack of investigation on the effect of thermal oxidation on morphological characteristics of substrate materials. In this study, the cordierite (Cord) and attapulgite (ATP) powders were mixed with CeO_2, serving as substrate and catalyst, respectively. The soot particles were collected from a heavy-duty diesel engine. Through the thermal oxidation from 450 to 650 ℃, it was found that the special fibrous or rod-like structure of ATP produced more pore volume and surface area, as well as an efficient heat recovery mechanism after thermal oxidation. The block-like structure of Cord only acted as a substrate, maintaining its intact crystalline structure during thermal oxidation. Notably, the oxidation reactivity of ATP/CeO_2/Soot was higher than Cord/CeO_2/Soot because the ATP generated more catalyst active sites and sufficient contact area for the soot-oxygen-CeO_2 reaction. This study expands the potential application of ATP as DPF substrate material.

Keywords: Diesel engine; Attapulgite; Heat recovery; Morphology; Soot oxidation

1. Introduction

Diesel particulate matter contributes to serious environmental issues including haze and photochemical smog. The diesel particulate filter (DPF) showed significant potential for particulate reduction and typically achieving filtration efficiencies exceeding 95% [1]. In DPF, the soot particle layer must be removed by regeneration either periodically or continuously to prevent the increase of backpressure and fuel consumption [2, 3]. The active regeneration involved by soot particles burning above 550 ℃ in exhaust. The DPF regeneration process was a complex and endothermic reaction process. The catalyst substrate structural characteristics were affected by heat release during regeneration [4-6].

In order to improve active regeneration performance of DPF, the thermal management for parallel channels has been widely researched [7,8]. Yu et al. [9] reported that the DPF heat transfer properties depend on the heat capacitance ratio and the hydraulic parameters. With the decrease of the DPF substrate thickness, the speed of the temperature front was improved. Fang et al. [10] suggested that the peak substrate temperature of substrate material was affected by regeneration temperatures, while decreasing exhaust flow rate and improving regeneration temperature resulted in higher peak substrate temperature and maximum temperature gradients. Lee et al. [11] reported that the thermal capacity and heat transfer rate of DPF parallel channels were influenced by oxygen concentration and maximum wall temperature. Higher oxygen concentration led to thermal failure, while higher soot deposition with the higher

regeneration temperature produced the best regeneration performance [12]. Meng et al. [13,14] cordierite structure could change to some extent at high temperature, which affected the filtration efficiency. High temperature airflow and microporous expansion enhanced particle penetration.

The materials used for manufacturing DPF played an important role in regeneration process [8,15]. The channels of DPF consist of porous substrate material included cordierite, silicon carbide, acicular mullite, aluminum titanate, metal foams and fibers [16]. Cordierite (abbreviated hereafter as Cord), derived from a mixture containing clay [$Mg_2Al_4SiO_{18}$], served as the primary component of DPF catalyst substrate. It was reported that the Cord is known to form at high temperature sintering method, which has a dense microstructure with evenly distributed grains and few small pores [17]. The Cord had favorable thermal expansion coefficient and resistance to cracking from material fatigue, and an excellent thermal shock resistance [18-21]. Xu et al. [22] mentioned that the flow uniformity and pressure drop of DPF channels were affected by the permeation resistance of the Cord substrate material. It has been confirmed that cordierite mixed with a small amount of CeO_2 showed unique oxygen storage capacity, which was recommended as a suitable catalytic converter for regeneration [23-25]. Zeng et al. [26] found that CeO_2 nanoparticles could provide a higher surface area without any heat treatment. The CeO_2 could be uniformly distributed across the interconnected pores of cordierite. Liu et al. [27] reported that the incorporation of CeO_2 facilitated the phase transformation of Cord, increasing permeability and larger pore sizes. In addition, to promote solid–solid interaction, some

new morphologies of ceria-based catalyst have been proposed, such as fibers, sticks, flakes, cubes, rods and stars. Among them, fibrous morphology was the best one for passive regeneration [28]. Zhang et al. [29] suggested that aluminum borate whiskers with cilia-like microstructure improved soot capture ability and low-temperature catalytic oxidation ability of soot. The filter efficiency, trapped soot particle distribution and catalyst content were affected by porous media in substrate material [30,31].

To improve temperature resistance and regeneration performance, researchers have continuously explored new carrier materials. At present, research on DPF substrate material was mainly focused on structural parameters [32-36]. Attapulgite (hereafter abbreviated as ATP) is a type of hydrated magnesium-aluminum silicate mineral [$(H_2O)_4(Mg,Al,Fe)_5(OH)_2Si_8O_{20}\cdot 4H_2O$] [22]. ATP has been widely used as catalyst substrate material because of its larger surface area, pore volume and thermal stability [37,38]. Cao et al. [39] demonstrated that the CuO catalyst doped over ATP showed good catalytic activity and thermal stability for CO oxidation. Zhu et al. [40] found that TiO_2 coated on ATP has been utilized to remove gaseous carbon disulfide (CS_2) from air. Larger surface area of ATP improved CS_2 removal efficiency. Additionally, ATP was employed as a catalyst support to remove diesel engine NOx emission, showing excellent performance [41].

The most direct influence on soot oxidation behavior is the contact point, which is determined by substrate material. However, there is a lack of investigation on structural changes of catalyst substrate material during thermal oxidation treatment. The larger surface area and pore volume of ATP were favorable for soot particle

deposition and catalytic reaction. Therefore, this study aimed to comprehensively evaluate the effect of thermal oxidation on morphological characteristics of Cord and ATP using various characterization techniques. Four types of ATP and Cord substrates were tested by thermal oxidation. The results revealed the impact of thermal oxidation on morphology, surface structure, crystalline structure and graphitization degree of substrate material. Additionally, the catalytic performances of CeO_2 coated on ATP and Cord were evaluated.

2. Experimental methodology

2.1 Experiment material

In present study, for thermal oxidation reaction, CeO_2 powder (99.99% purity, Sinopharm Chemical Reagent Co. Ltd., Shanghai, China) was selected as catalyst. It was reported that the CeO_2 catalyst doped over Cord exhibited significant oxygen storage capacity, appropriate porosity, flexural strength and thermal expansion coefficient [42,43]. The ATP powder, characterized by an average crystal diameter of 40~50 nm and honeycomb pore dimension measuring 0.38 nm × 0.63 nm, was produced from Gansu RongWan Science and Technology Co., Ltd. Cord powder was produced from Henan Hengyang Refractory Materials Co., Ltd., Henan, China. The ATP and Cord clays were used without any further purification, which were used as the porous substrates in this study. The ATP and Cord powders were selected based on their mesh sizes, specifically 200 mesh (particle diameter: 74 μm) and 325 mesh (particle diameter: 46 μm), respectively. A series of ATP/CeO_2 or Cord/CeO_2 samples were obtained so-called tight-contact mode by a pestle to grind carrier for 5 min, which

111 was synthesized by mechanical grinding method. The mass ratio of substrate and CeO_2
112 was prepared by 1/1 (100 mg/100 mg).

113 The most direct influence on soot oxidation behavior was the contact point
114 between soot particle, catalyst and substrate, which was difficult to research in molded
115 DPF filter [44,45]. Some researchers have evaluated catalyst activity towards soot
116 oxidation by powder form due to its superior dispersion [46,47]. The powdered Cord
117 and ATP as substrate material increased the effective contact area between soot
118 particles and catalyst. The interaction between the microstructure of catalyst substrate
119 and thermal oxidation could also be observed visually. In order to figure out the effect
120 of mechanical grinding on particle sizes of ATP and Cord, the effect of mechanical
121 grinding on particle size were analyzed by laser particle size distribution instrument
122 (BT-9300H), which has been listed in Fig. 1. It was shown that the volume mean
123 diameter of ATP/CeO_2 and Cord/CeO_2 decreased by 1-2 μm after mechanical grinding.
124 The particle size of the Cord and ATP samples remained unchanged, which had little
125 effect on the experimental results. The substrate/CeO_2 samples are named as
126 ATP200/CeO_2, ATP325/CeO_2, Cord200/CeO_2 and Cord 325/CeO_2.

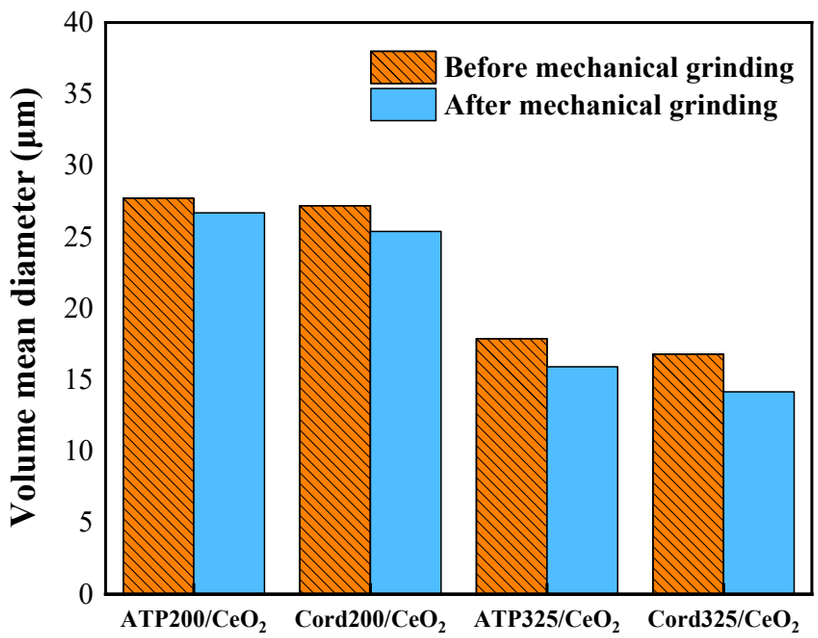

Fig. 1. Volume diameter of substrate/catalyst samples before and after mechanical grinding.

A heavy-duty diesel engine was employed to generate soot particles under steady-state condition (1500 r/min and 200 Nm). A comprehensive description of engine setup along with the sampling system is illustrated in Fig. 2. The engine specifications are detailed in Table 1. Soot particles were collected from the raw exhaust using 47 mm quartz fiber filters (2500QRT-UP, PALL) equipped with an automated filter support. The quartz fiber filters exhibited a precision of 0.3 μm with an aerosol retention rate of 99.9%. The sampling temperature was maintained at 55 ± 3 °C, with sampling duration of 90 min and sample flow rate of 1 L/s. In order to get enough samples for further analysis, the sampling time was controlled at 2 hours or longer. Subsequently, the particles attached to the filter paper surface were carefully scraped off from the paper filters. During this process, the filter paper was guaranteed not to be damaged, and the interference of filter paper could be removed. To prevent atmospheric moisture from

affecting the samples, the soot particle samples were stored in a desiccator after each measurement [48]. There pre-treatments like ultrasonic wave treatment and centrifugal separation in dichloromethane solvent were not employed in this study [49].

In order to simulate soot oxidation real DPF channels, the powdered soot particle and substrate/catalyst sample were mixed by gently shaking with a vortex mixer for 2 min at a weight ratio of 1:10 (10 mg of soot particle to 100 mg of substrate/catalyst), which was named as loose-contact mode and be employed in many literatures [50-53]. When the soot particles trapped inside the DPF channels, the oxidation rate of soot was related to the effective contact area of the catalyst [54,55]. The experimental method employed in this study revealed the difference of contact conditions between Cord, ATP, CeO_2 and soot particles. The key influencing the catalytic performance was the porosity in the DPF substrate [56,57]. The powdered soot-substrate mixtures could provide the influence of substrate material porous structure on intrinsic activity of catalyst materials. The samples were labeled as ATP200/CeO_2/Soot, ATP325/CeO_2/Soot, Cord200/CeO_2/Soot and Cord 325/CeO_2/Soot.

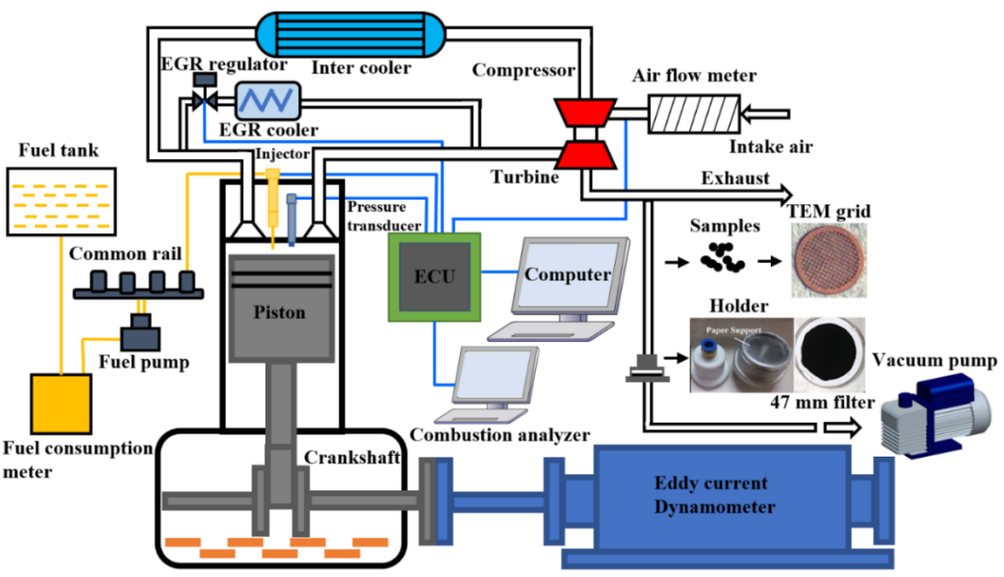

158 **Fig. 2.** Schematic diagram of the engine set-up and sampling system

159 **Table 1** Engine specifications

Categories	Properties
Number of cylinders	4
Max speed	2800 r/min
Stroke	118 mm
Bore	102 mm
Compression ratio	17:1
Valves per cylinder	4
Displacement	3.865 L
Fuel injection system	Common rail direct injection

160 **2.2 Characterization methods**

161 The morphological characteristics analyzed in this study mainly include
162 morphology, surface structure, crystalline structure and graphitization degree. The
163 morphology was characterized by scanning electron microscopy (SEM, Hitachi
164 Regulus 8100, Japan), coupled with energy dispersive spectroscopy (EDS, INCA-350,
165 Oxford, UK). EDS was employed to examine the elemental distribution on sample
166 surface. The surface area and total pore volume were determined through N_2
167 physisorption under -196 °C using Micromeritics TriStar II 3030 (USA), in accordance
168 with the Brunauer-Emmett-Teller (BET) method for physical adsorption, as well as the
169 Barrett-Joyner-Halenda (BJH) method for pore diameter. The crystalline structure of
170 sample was analyzed using X-ray diffraction (XRD, Bruker AXS D8-Focus, Germany).
171 Standard Cu/Kα radiation (λ = 0.154 nm) was utilized at 40 kV and 40 mA, covering a
172 scanning range of 3º to 90º. The standard compounds reported in the JCPDS database
173 were employed to identify the diffraction peaks corresponding to the crystalline phases,
174 which primarily facilitated the identification of mineral phases. Qualitative analysis
175 was performed by the MDI Jade 6.0 computer program.

Table 2 The TGA specific heat-up program

Stages	Descriptions
0	Samples in nitrogen
1	Initial temperature 25 ℃
2	Ramp 10 ℃/min to 450 ℃
3	Isothermal for 30 min
4	Air introduced
5	Ramp 2.5 ℃/min to 650 ℃

The soot graphitization degree was assessed by Raman analysis. The first-order original spectrum of the substrate/catalyst sample was obtained through Raman spectrometer with a wavelength of 514.5 nm and source power of 9.3 μW. The low-pressure atomic line lamp was used to calibrate the spectral resolution of the Raman spectrometer. The soot oxidation rate was analyzed using ZCT-A Simultaneous Thermal Analyzer. The thermal treatment is listed in Table 2. The volatile organic fraction, which was mainly consisted of organic carbon, could be removed by thermal treatment [58,59]. To remove organic carbon, the soot particle sample was heated to 450 °C and then maintained for 30 min, utilizing high-purity nitrogen as protective gas. During the oxidation stage, air was introduced as oxidizing gas with the temperature increasing from 450 to 650 °C, ensuring complete oxidation during the regeneration process [60]. Additionally, partially oxidized soot samples with a conversion rate of 50% were obtained for further characterization, which were named as ATP200/CeO_2/Soot-oxidized 50%, Cord200/CeO_2/Soot-oxidized 50%, ATP325/CeO_2/Soot-oxidized 50% and Cord325/CeO_2/Soot-oxidized 50%. All results were expected to provide information about the morphological characteristics of Cord and ATP during the

193 thermal oxidation.

194 **3. Results and discussion**

195 **3.1 Characterization of substrate/catalyst**

196 To better understand the changes of morphology and nanostructure during
197 oxidation thermal, the morphology and elemental composition of ATP/Cord doped over
198 CeO_2 were analyzed by SEM-EDS. The Fig. 3 illustrates the typical images of
199 ATP200/CeO_2, ATP325/CeO_2, Cord200/CeO_2 and Cord 325/CeO_2 without thermal
200 treatment. High magnification images were employed to analyze morphological
201 relationship between substrate and soot, revealing significant differences in texture, size
202 and dispersion. All samples exhibited numerous typical fibers approximately 0.5 to 2
203 μm in length, arranged into bundles. The morphology of ATP clay confirmed the
204 fibrous or rod-like structure. The whisker-like surface was believed to enhance soot
205 particle filter. On the other hand, the Cord displayed a block-like structure with some
206 clumps and smooth surfaces, which was associated with its slipperiness. The
207 morphology of Cord showed varying degrees of micro-cracking.

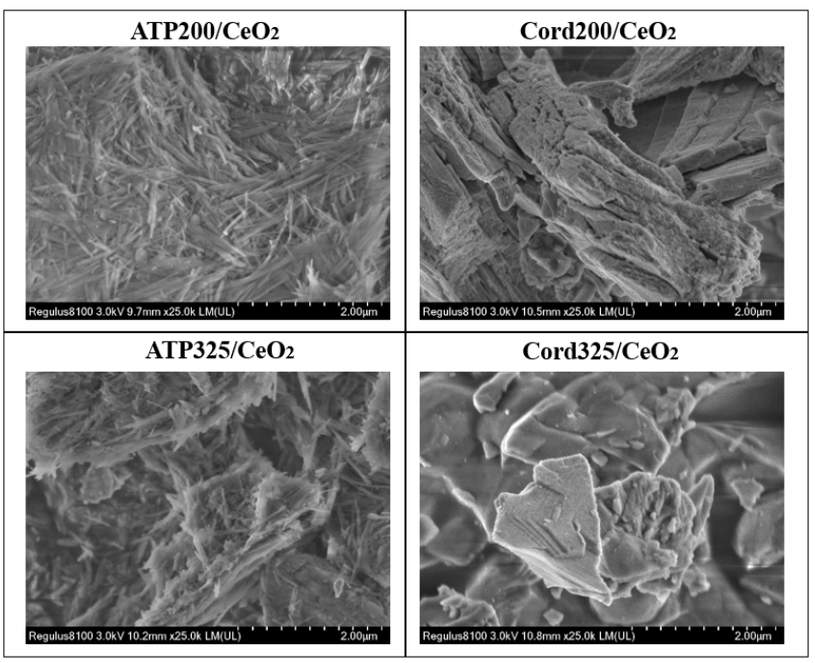

208

209 **Fig. 3.** SEM images for substrate/catalyst samples.

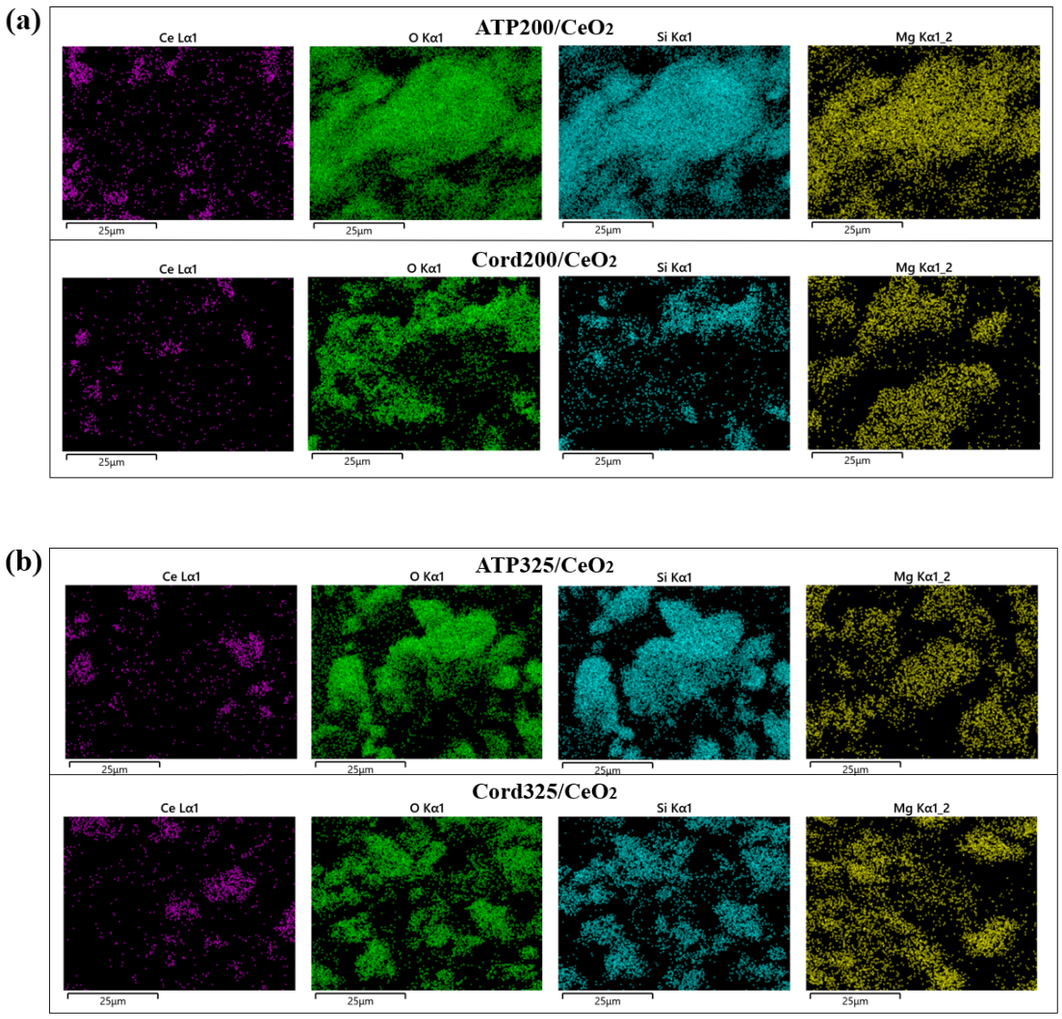

Fig. 4. Elemental mapping for catalyst/substrate samples.

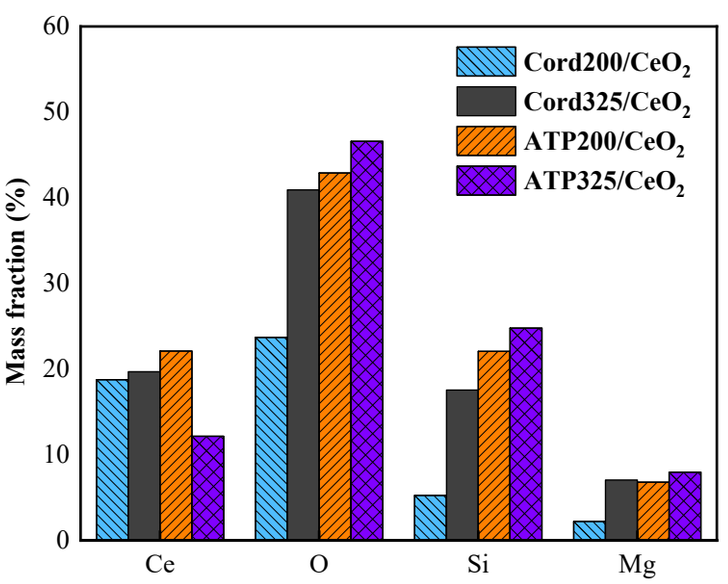

Fig. 5. The elemental mass fraction in catalyst/substrate samples.

To identify and trace the clay and catalyst elements in the ATP/Cord, EDX mappings were conducted for each sample. The Fig. 4 shows the elemental analysis results of ATP200/CeO_2, ATP325/CeO_2, Cord200/CeO_2 and Cord 325/CeO_2. The mass fractions of Ce, O, Si and Mg are listed in Fig. 5. The Ce (pink) was totally from CeO_2 catalyst which was tightly contacted with ATP/Cord by grinding method. The electron probe moved over the surface in raster fashion, and a map of surface composition was conducted. The EDS could reveal the element distribution and concentration on the sample surface. The fibrous or rod-like structure of ATP produced higher surface area and pore volume, which promote the CeO_2 to enter the pores. However, due to the block-like structure of Cord, the catalyst particles mainly distributed on Cord surface. Therefore, the Cord might display higher relative content of Ce in EDS mapping. The distribution of cerium was more compact and uniformly shaped, indicating higher concentration and intensity. The CeO_2 coated on substrate external surface demonstrated a better catalytic performance. The Si (blue) and Mg (yellow) signals were generated by compositions presented in Cord and ATP substrates. As anticipated, Si (blue) and O (green) elements were two dominant in ATP/Cord, which shared the same spots in EDS mapping. For ATP and Cord silicate minerals, there were similar distribution for these four elements. The O was the most abundant element for all samples. It was clearly that the relative content of Ce element in Cord was bigger than it in ATP due to smaller molecular mass of Cord material.

3.2 Thermal oxidation behavior

To analyze the change of morphology and nanostructure of ATP and Cord during thermal treatment, the oxidation tests from 450 to 650 ℃ were conducted on TGA. The normalized mass loss versus temperature curves of ATP200/CeO_2/Soot, Cord200/CeO_2/Soot, ATP325/CeO_2/Soot and Cord325/CeO_2/Soot are presented in Fig.

6. Comparing with Cord, the ATP resulted in notable leftward shift of mass loss curves, indicating an enhancement on soot oxidation. The oxidation behavior of diesel soot was also tested. Obviously, the Cord or ATP mixed with CeO_2 showed higher soot oxidation reactivity than diesel soot.

The temperatures defined as T10, T50, and T90 corresponded to soot samples with 10%, 50%, and 90% mass loss, respectively. Lower characteristic temperature indicated that higher oxidation rate [61,62]. As shown in Table 3, when the Cord was replaced by ATP, the T10, T50, and T90 for 200 mesh samples decreased by 15.9 °C, 13.7 °C and 13.1 °C, respectively. For 325 mesh samples, the T10, T50 and T90 decreased by 6.6 °C, 15.3 °C and 11.2 °C, respectively. In addition, to quantitatively evaluate the oxidation reactivity of soot samples, activation energy (*Ea*) was derived from TGA curve through the Arrhenius model in Eq. (1).

$$-dm/dt = A \cdot exp(-Ea/RT) \cdot m^n \cdot P^r \quad (1)$$

where t is the reaction time; m is the instantaneous mass of soot sample; A is the preexponential factor; Ea is the activation energy; R is gas constant; T is the reaction temperature of soot sample; n is reaction order, which is considered as 1; P and r are partial pressure and reaction order of oxygen, respectively. The reaction order of oxygen is determined to be 1 by referring to the previous studies [63-65]. Eq. (1) can be rearranged as:

$$ln(-dm/mdt) = ln(AP) - Ea/RT \quad (2)$$

where the oxidation kinetic parameters, Ea and A, are estimated from the slope and intercept of $ln(-dm/mdt)$ against $1/T$, respectively. The calculations of soot-

oxidation kinetic analysis were shown in Fig. 7. As shown in Table 3, for ATP200/CeO_2/Soot, the *Ea* value is 138.6 kJ/mol, and 152.6 kJ/mol for the Cord200/CeO_2/Soot, 134.4 kJ/mol for the ATP325/CeO_2/Soot, 144.5 kJ/mol for the Cord325/CeO_2/Soot. The *Ea* value of diesel soot is 178.9 kJ/mol, indicating that the lowest soot oxidation reactivity. It can be seen the *Ea* with the order: ATP < Cord. Higher *Ea* indicated lower oxidation reactivity, indicating more resistance towards oxidation. The soot oxidation mechanism primarily depended on the reactive oxygen species at catalyst-soot contact points. The CeO_2 coated on ATP produced rich array of active oxygen catalytic sites, along with sufficient reaction surface area. In addition, the well-dispersed nanostructure of ATP produced more contact points between CeO_2 and oxygen, allowing it to reversibly exchange oxygen through oxidation reaction.

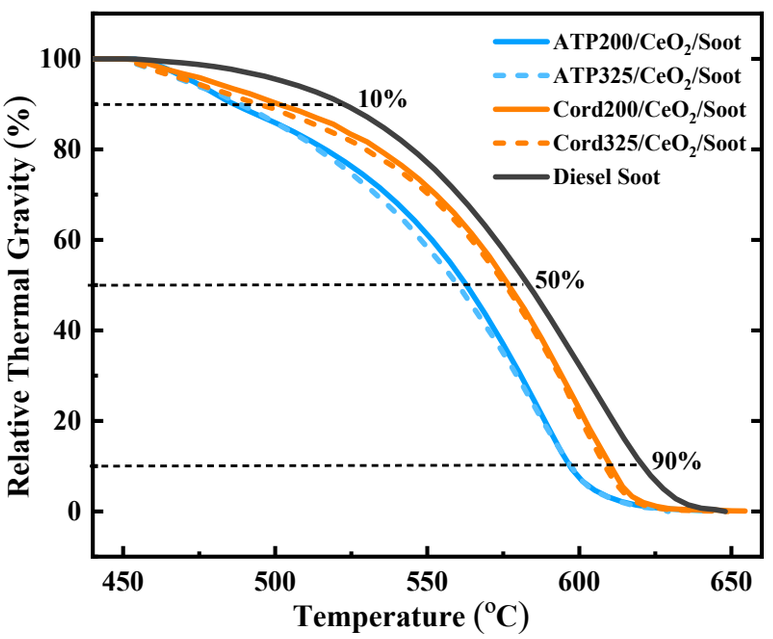

Fig. 6. Thermogravimetric analysis for soot samples.

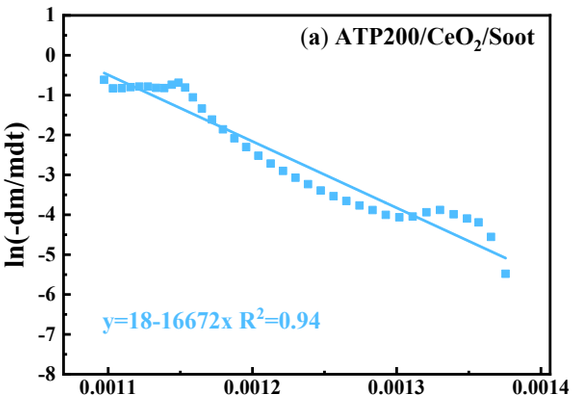

275

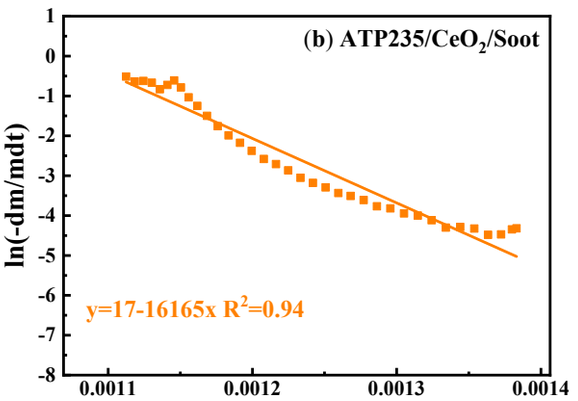

276

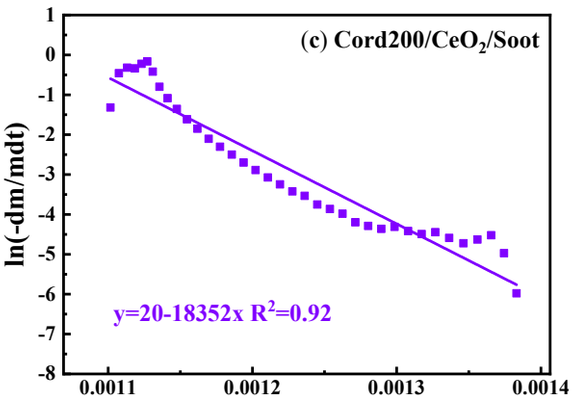

277

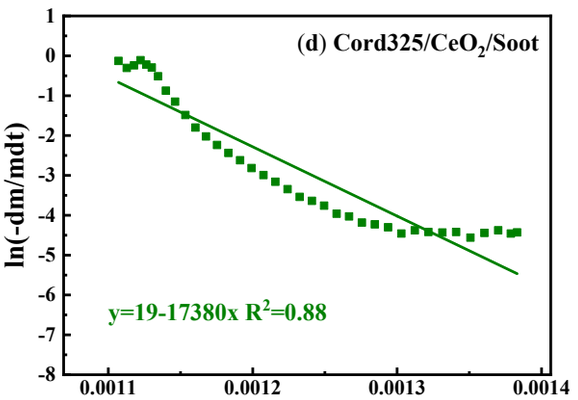

278

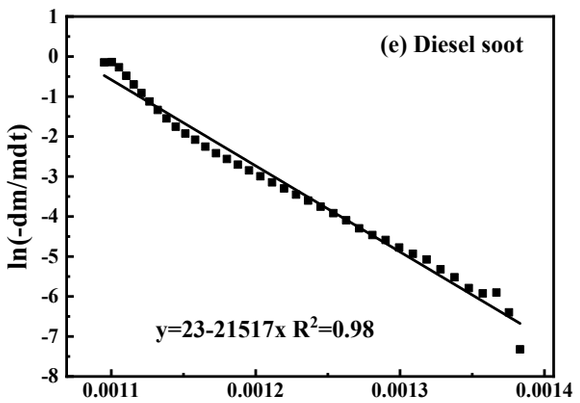

Fig. 7. Soot-oxidation kinetic analysis based on an Arrhenius mode.

Table 3 Oxidation characteristic temperature and activation energy (*Ea*)

Samples	T10 ℃	T50 ℃	T90 ℃	*Ea* (kJ/mol)
Cord200/CeO_2/Soot	501.6	576.6	609.8	152.6
Cord325/CeO_2/Soot	495.2	575.7	608.8	144.5
ATP200/CeO_2/Soot	485.7	562.9	596.7	138.6
ATP325/CeO_2/Soot	488.6	560.4	597.6	134.4
Diesel Soot	522.9	583.7	620.5	178.9

3.3 Morphology changes during thermal oxidation

3.3.1 SEM morphology

Shorter distance and more contact points between soot and catalyst represented better catalytic performance of substrate porous material [66]. Consequently, it was essential to investigate the morphology changes of ATP and Cord during thermal oxidation process. The Fig. 8 shows typical SEM images of ATP200/CeO_2/Soot, Cord200/CeO_2/Soot, ATP325/CeO_2/Soot and Cord325/CeO_2/Soot under different oxidation degrees (0%, 50% and 100%).

In Fig. 8 (a) and (c), the enlarged images revealed that ATP was primarily consisted of irregularly arranged rod-shaped structures. The yellow dotted lines were

293 employed to completely circle the diesel soot particles in SEM images. The dispersed
294 soot particle aggregates were uniformly distributed within the ATP, ranging from 0.4-
295 1.2 μm. A careful observation showed an important finding that most soot particle were
296 captured by the rod-like structure of ATP, which was favorable with the contact
297 between soot, CeO_2 and oxygen. At oxidation degree of 50%, ATP whiskers became
298 fewer in number and more scattered. Along with thermal oxidation, the diameter of soot
299 particle aggregate decreased to 0.2-0.6 μm. After thermal treatment, the morphology of
300 ATP was back to before its thermal oxidized, indicating better consistency of catalytic
301 performance. The change of fibrous or rod-like structure could be ignored. As shown
302 in Fig. 8 (b) and (d), the soot particles on Cord displayed uniform and dense distribution.
303 Obviously, along with thermal oxidation, the dense soot particle distribution gradually
304 decreased obviously. Before oxidation, the diameter of soot particle aggregate was
305 above 3 μm, completely covered by substrate material. At oxidation degree of 50%, the
306 surface soot particles were oxidized, the aggregate size decreased at least 1 μm.
307 Comparing with ATP, the block-like structure of Cord only acted as a substrate, and
308 did not promote the contact between soot, oxygen and CeO_2 catalyst.

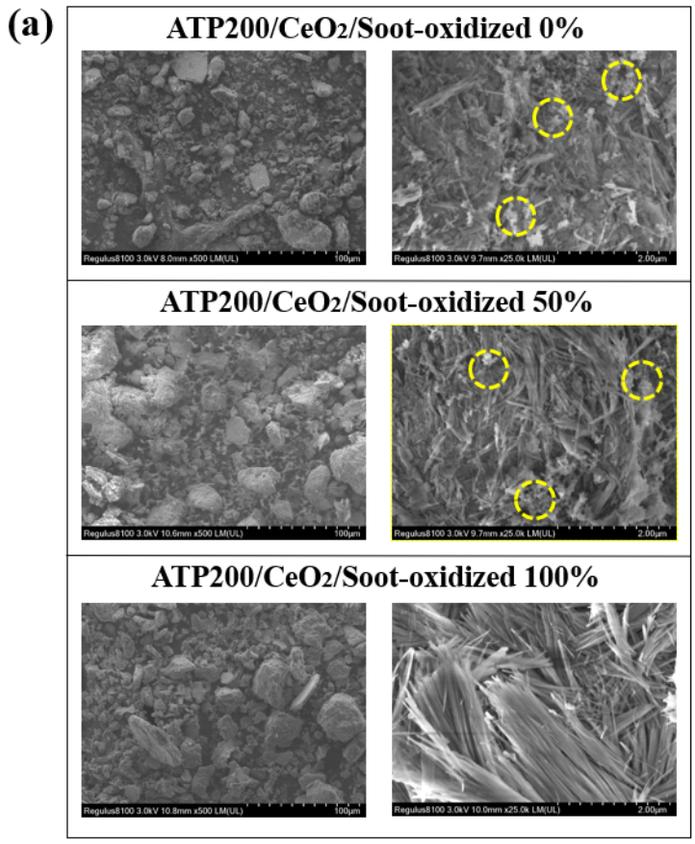
(a)
ATP200/CeO2/Soot-oxidized 0%
ATP200/CeO2/Soot-oxidized 50%
ATP200/CeO2/Soot-oxidized 100%

309

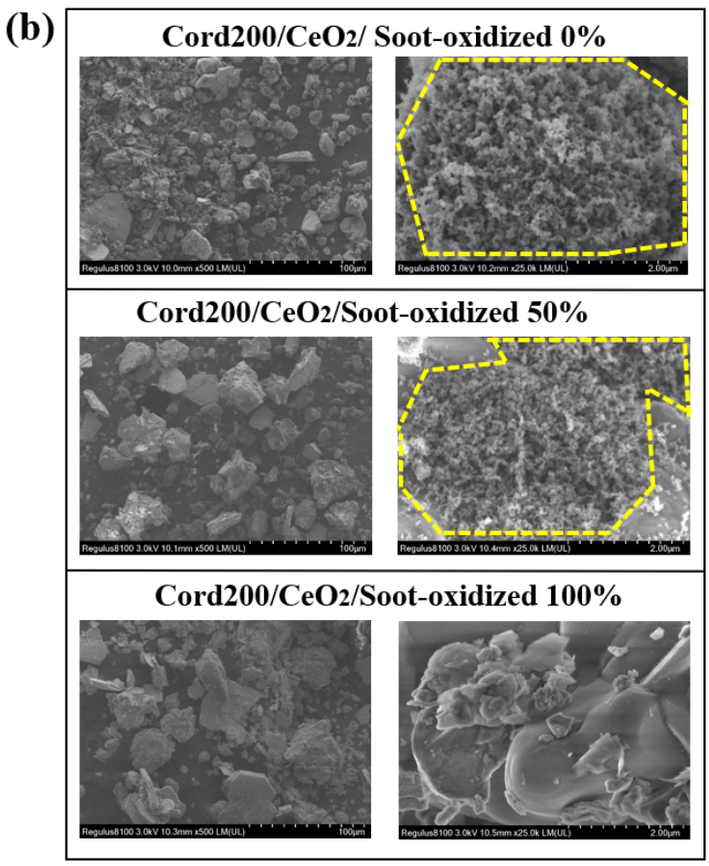
(b)
Cord200/CeO2/ Soot-oxidized 0%
Cord200/CeO2/Soot-oxidized 50%
Cord200/CeO2/Soot-oxidized 100%

310

(c)

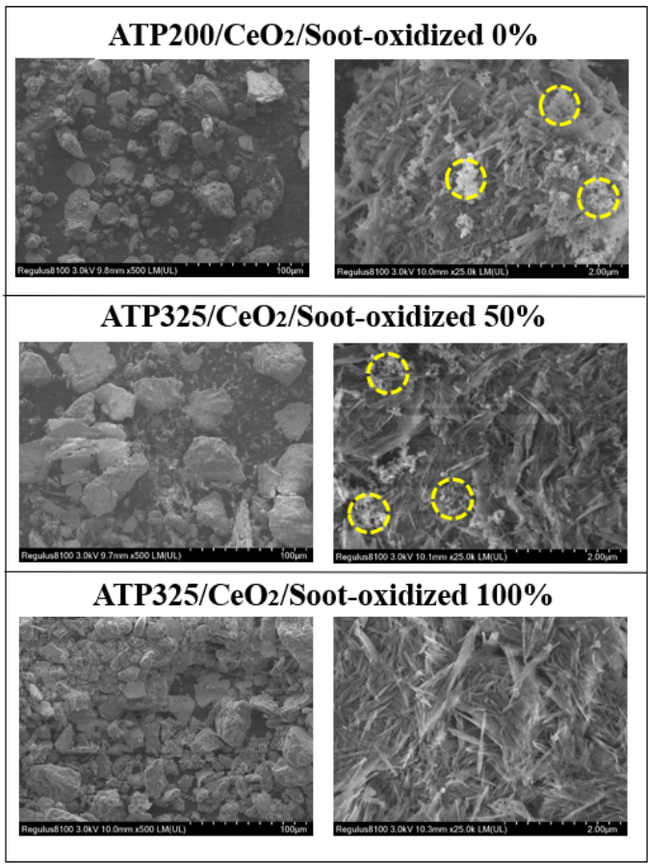
ATP200/CeO2/Soot-oxidized 0%
ATP325/CeO2/Soot-oxidized 50%
ATP325/CeO2/Soot-oxidized 100%

311

(d)

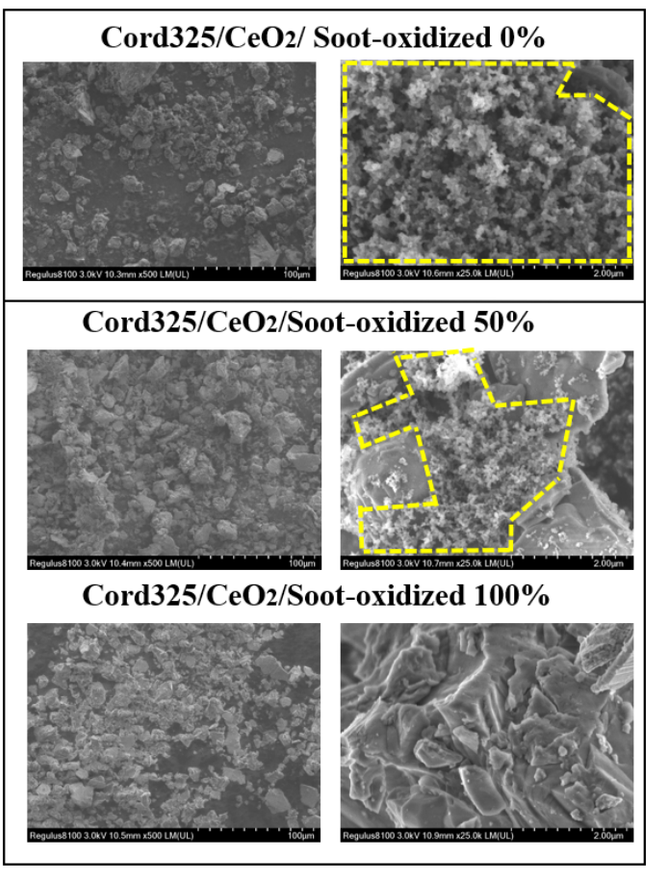
Cord325/CeO2/ Soot-oxidized 0%
Cord325/CeO2/Soot-oxidized 50%
Cord325/CeO2/Soot-oxidized 100%

312

313 **Fig. 8.** SEM morphology for substrate/ catalyst samples

314 *3.3.2 Surface structure*

315 To better understand the correlation between surface structure and catalytic
316 performance, the surface structures of ATP200/CeO_2/Soot, Cord200/CeO_2/Soot,
317 ATP325/CeO_2/Soot and Cord325/CeO_2/Soot were analyzed by BET. As shown in Fig.
318 9, the surface area and total pore volume of ATP are significantly larger than Cord
319 before and after oxidation, respectively. The special fibrous or rod-like structure of ATP
320 produced more pores with the increase of surface area. The block-like structure of Cord
321 had a relatively poor pore-forming capacity. Along with thermal oxidation, for each of
322 sample, the pore diameter increased, but pore volume decreased. The clay mesh number
323 had no obvious effect on pore volume. The pore volume and surface area decreased
324 which was caused by the thermal sintering.

325 There was a clear correlation between soot thermal oxidation temperature and
326 specific surface area. The soot oxidation temperature of substrate/catalyst sample
327 decreased with increased surface area and pore volume, which were beneficial for
328 catalytic oxidation performance. Higher surface area increased the number of active
329 catalytic site, thereby enhancing the soot oxidation reaction. The CeO_2 catalyst
330 generated more active sites, oxygen species and a stronger dispersion of active
331 components by large surface area of ATP, which improved the residence time and
332 deposition rate of soot particle. The interaction between soot particle, active site and
333 active oxygen species was enhanced by the increased surface area, resulting in higher
334 oxidation activity. Consequently, a fine and uniform distribution of CeO_2 was achieved
335 due to the large specific surface area and smaller pore size. These results well explained
336 why soot particles coated on ATP had better oxidation reactivity.

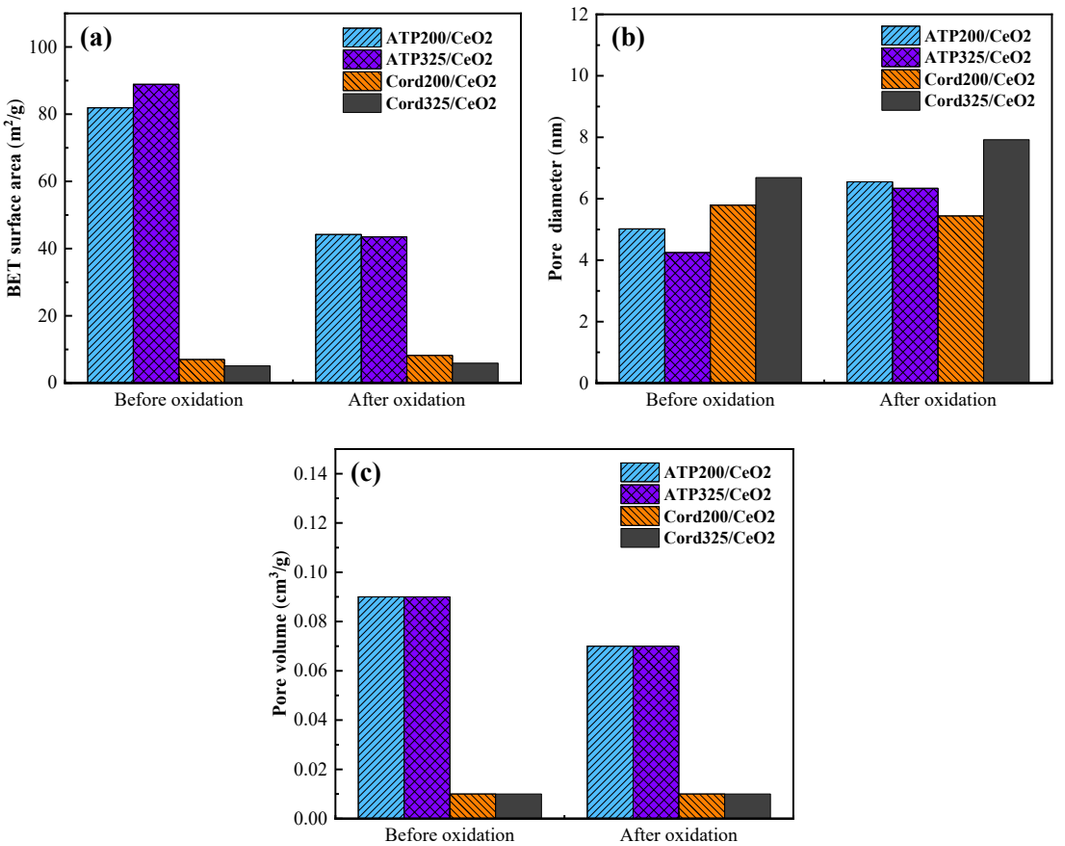

Fig. 9. Surface structure of substrate/catalyst samples before and after oxidation: (a) Surface are, (b) Pore diameter and (c) Pore volume.

3.3.3 Crystalline structure

In order to analyze the impact of thermal oxidation on ATP and Cord structures, quantitative crystalline information was obtained by XRD. The XRD patterns of substrate/catalyst samples under oxidation degrees of 0% and 50% are depicted in Fig. 10. The characteristic peak positions observed at 8.5°, 19.9° and 26.6° correspond to the (110), (040) and (400) planes of ATP clay, respectively [67]. Due to the high degree of ATP crystallinity, the most intense peak was located at 26.6°. The diffraction peak observed at 8.5° was attributed to the basal spacing of ATP framework. The peak at 8.5° nearly disappeared after 50% partial oxidation, as evidenced by its markedly low

intensity. The diffraction peak at near 8.5° was a characteristic peak of ATP, which is different from other minerals. The (110) diffraction peak of ATP at 8.31° weakened after hydrothermal reaction with a more obvious decreasing of peak intensity, resulting from the partial collapse of the crystal framework [68]. The decreased intensity of ATP diffraction peak at 8.4° derived from the increase of calcination temperature. Therefore, this reduction was attributed to the decrease of the basal distance between interlayers of ATP by thermal oxidation. Diffraction peaks at 28.5°, 33.0°, 47.5° and 56.4° corresponded to the (111), (200), (220), and (311) planes of CeO_2, respectively. These peaks exhibited a cubic fluorite structure, in accordance with the standard JCPDS card number 34-0394 [69]. During the thermal oxidation, the XRD pattern of CeO_2 showed no significant changes, indicating the stability of the ATP/CeO_2 catalytic performance.

As illustrated in Fig. 10 (b), peaks located at 10.5°, 21.8°, and 26.4° are associated with (110), (112) and (132) planes of Cord clay, respectively, based on JCPDS card number 12-0303 [70]. The characteristic peaks of Cord remained unchanged before and after thermal oxidation, confirming the structural integrity of its crystalline framework. The block-like structure of Cord was not affected by thermal oxidation reaction. Notably, the CeO_2 exhibited the highest lattice strain, which correlated with its elevated catalytic activity. The intensity of the CeO_2 diffraction peaks corresponding to (200) and (311) slightly decreased after thermal treatment. When CeO_2 was doped onto Cord, the particle size and crystal structure of CeO_2 were influenced by thermal oxidation.

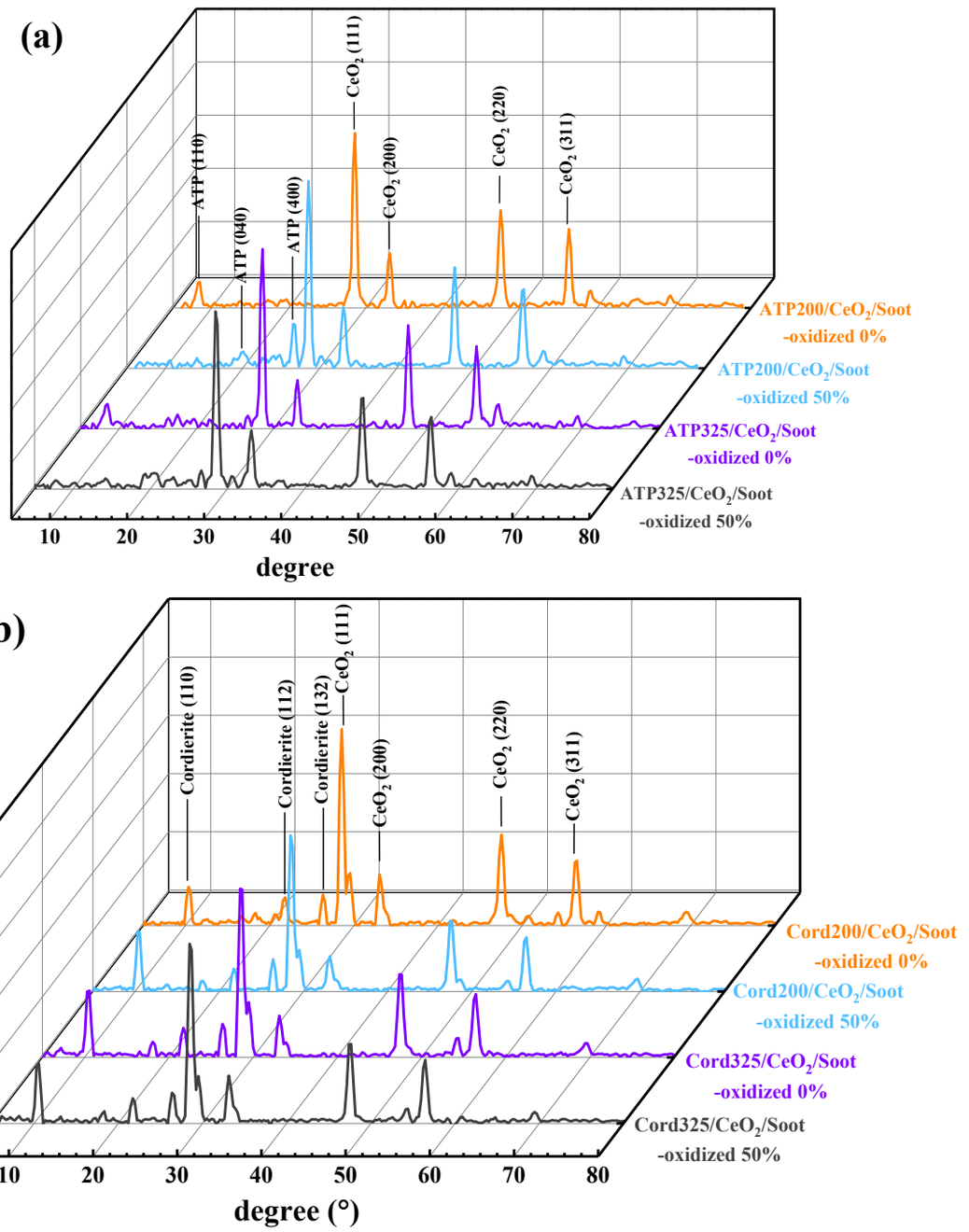

Fig. 10. XRD patterns of substrate/catalyst samples under 0% and 50% oxidation degrees: (a) ATP and (b) Cord.

3.3.4 Graphitization degree

To supplement the nanostructure information of substrate/catalyst samples, the graphitization degree was assessed by Raman analysis. As illustrated in Fig. 11, the 3L1G method is employed for Raman spectrum curves fitting, which includes three

Lorentzian bands at approximately 1590 cm^{-1} (G band), 1360 cm^{-1} (D1 band) and 1200 cm^{-1} (D4 band), along with a Gaussian band near 1500 cm^{-1}. The peak intensity of G band corresponds to the in-plane bond stretching vibrations of ideal graphite, whereas the D band is related to lower or minimal symmetry in hexagonally structured crystals [71]. The relative ratios of D1 and G band areas (A_{D1}/A_G) are presented in Table 4, with standard errors derived from three repeated tests. Some researchers have demonstrated that a lower A_{D1}/A_G ratio represented higher graphitization degree of sample nanostructure [72,73].

With a conversion rate of 50%, all of the A_{D1}/A_G values significantly decreased, indicating the increase of soot graphitization degree. During thermal oxidation, the number of graphite carbon layer increased with typical shell/core shape, consisting of inner-core region and outer shell formed by well-ordered carbon layer [60]. The certain functional groups between the carbon layers were removed, resulting in a more ordered graphitic lattice structure [74]. In this study, the difference of A_{D1}/A_G between 0% and 50% oxidation degrees represented the soot aging degree. Notably, the A_{D1}/A_G difference of ATP sample was bigger than that of Cord. This indicated that the CeO_2 coated on ATP had better catalytic performance because of higher oxygen capacity and more active sites. This results also verified the thermal oxidation behavior in Section 3.2.

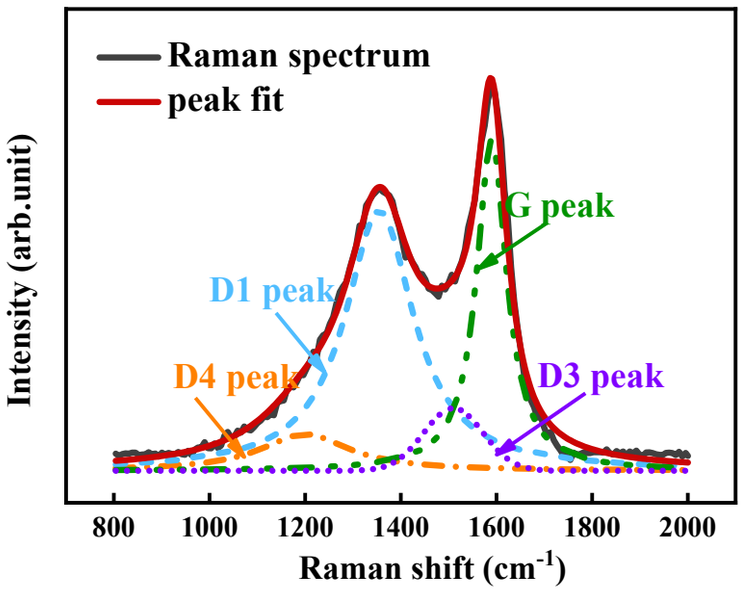

Fig. 11. Raman spectrum analysis and curve fit.

Table 4 Ratios of A_{D1}/A_G for samples

Samples	A_{D1}/A_G	Std.
ATP200/CeO_2/Soot-oxidized 0%	2.76	0.1
Cord200/CeO_2/Soot-oxidized 0%	2.43	0.01
ATP325/CeO_2/Soot-oxidized 0%	2.46	0.09
Cord325/CeO_2/Soot-oxidized 0%	2.5	0.04
ATP200/CeO_2/Soot-oxidized 50%	2.22	0.03
Cord200/CeO_2/Soot-oxidized 50%	2.33	0.01
ATP325/CeO_2/Soot-oxidized 50%	2.08	0.04
Cord325/CeO2 /Soot-oxidized 50%	2.36	0.03

Based on the above analysis of morphology characteristics, there was an efficient heat recovery mechanism after thermal oxidation for ATP. The SEM analysis of ATP revealed minor changes in the material's morphology microstructure. Before and after thermal oxidation, the irregularly arranged rod-shaped structures were always presented in ATP whiskers. Similarly, the block-like structure of Cord only acted as a substrate. The effect of thermal oxidation on the block-like structure of Cord could almost be

406 ignored. The XRD peak intensities of ATP characteristic peaks corresponding to (040)
407 and (400) planes and Cord characteristic peaks corresponding to (110), (112) and (132)
408 showed no changes after oxidized 50%, indicating better stability of crystalline
409 structure. Meanwhile, the peak intensities of CeO_2 characteristic peaks had no changes
410 before and after oxidation. To better evaluate the cyclic stability of substrate materials,
411 the BET analysis was performed before and after thermal oxidation. The change rates
412 of pore volume and pore diameter of Cord before and after thermal oxidation are less
413 than 15%. Although the surface area of ATP decreased from 81.9 to 44.2 m^2/g, it is also
414 significantly bigger than that of Cord. Therefore, in present study, both substrate
415 materials of catalyst demonstrated superior stability.

416 In summary, the position relationship between soot particle, oxygen and CeO_2
417 catalyst within the ATP and Cord substrates are illustrated in Fig. 12. The morphology
418 characteristics were critical factors in terms of catalytic performance. Comparing with
419 block-like structure of Cord, the fibrous or rod-like structure of ATP produced higher
420 surface area and pore volume, which could capture more soot particles because of its
421 higher specific surface area, pore volume, as well as higher capacity of CeO_2 catalyst
422 and oxygen molecules. On the other hand, the distances between soot, catalyst and
423 oxygen played a crucial role in catalytic reaction, which decreased by the fibrous or
424 rod-like structures of ATP, as well as higher catalytic activity. The fibrous morphology
425 was the best one for passive regeneration, which promoted solid–solid interaction. The
426 morphology of ATP showed special fibrous or rod-like structure. The solid–solid
427 interactions between CeO_2 catalyst and soot particles were enhanced by fibrous or rod-

like structure of ATP, indicating more complete catalytic reaction.

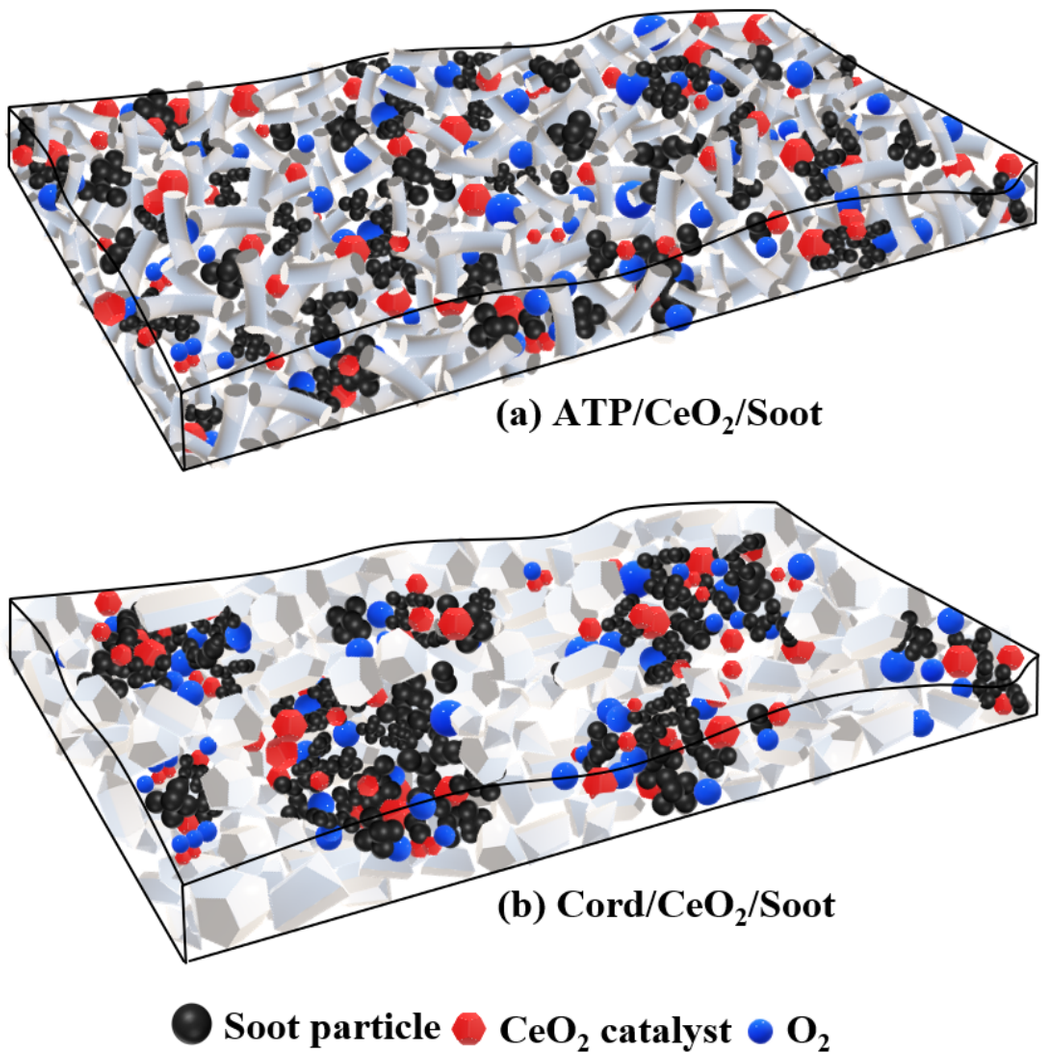

Fig. 12. Schematics of oxygen-soot-catalyst contact condition in different catalyst substrates of (a) ATP and (b) Cord

4. Conclusion

Based on thermal oxidation test, the morphological characteristics of ATP and Cord were measured. The main conclusions are as follows:

(1) The special fibrous or rod-like structure of ATP produced more pore volume and surface area. There was a heat recovery mechanism that the morphology of ATP

was back to what it was before thermal oxidation, indicating favorable consistency of catalytic performance. However, the basal spacing of ATP framework was reduced by thermal oxidation.

(2) Increasing the oxidation conversion led to the decrease of uniform and dense distribution of soot particle on Cord surface. The block-like structure of Cord only acted as a substrate, and does not promote the contact between soot, oxygen and CeO_2 catalyst. The XRD diffraction peak of Cord exhibited no changes before and after thermal oxidation, which confirmed that the crystalline structure of Cord remained intact during thermal oxidation.

(3) The ATP provided more active sites of catalyst and sufficient reaction surface area for the soot-O_2-CeO_2 reaction, resulting in higher soot graphitization degree. The oxidation reactivity of ATP/CeO_2/Soot system was higher than Cord/CeO_2/Soot system, in which a certain decrease of activation energy and characteristic oxidation temperatures.

The future research should focus on the comparison of structural stability and particulate filter efficiency between ATP and Cord. The difference of soot oxidation behavior between ATP and Cord in real DPF channels will be investigated.

Declaration of interest statement

The authors declare that they have no known competing financial interests or personal relationships that could have appeared to influence the work reported in this paper.

Acknowledgments

This work was supported by Key Research and Development Program of Gansu

Province (25YFWA015) and the Science and Technology Planning Project of Gansu Province (24CXGA049).

References

[1] J. Fang, Z. Meng, J. Li, Y. Du, Y. Qin, Y. Jiang, W. Bai, G.G. Chase, The effect of operating parameters on regeneration characteristics and particulate emission characteristics of diesel particulate filters, Appl. Therm. Eng. 148 (2019) 860-867. https://doi.org/10.1016/j.applthermaleng.2018.11066.

[2] Y. Shi, Y. Cai, R. Fan, Y. Cui, Y. Chen, L. Ji, Characterization of soot inside a diesel particulate filter during a nonthermal plasma promoted regeneration step, Appl. Therm. Eng. 150 (2019) 612–619.

[3] L. Lisi, G. Landi, V. Di Sarli, The Issue of Soot-Catalyst Contact in Regeneration of Catalytic Diesel Particulate Filters: A Critical Review, Catalysts. 10 (2020) 1307.

[4] Y.W. Deng, W.P. Zheng, J.Q. E, B. Zhang, X.H. Zhao, Q.S. Zuo, Z. Zhang, D.D. Han, Influence of geometric characteristics of a diesel particulate filter on its behavior in equilibrium state, Appl. Therm. Eng. 123 (2017) 61-73.

[5] H. Caliskan, K. Mori, Environmental, enviroeconomic and enhanced thermodynamic analyses of a diesel engine with diesel oxidation catalyst (DOC) and diesel particulate filter (DPF) after treatment systems, Energy. 128 (2017) 128-44.

[6] J. Benajes, A. García, J. Monsalve-Serrano, V. Boronat, An investigation on the particulate number and size distributions over the whole engine map from an optimized combustion strategy combining RCCI and dual-fuel diesel-gasoline, Energy. Convers. Manag. 140 (2017) 98-108.

[7] X. Zhao, J. Jiang, H. Zuo, G. Jia, Soot combustion characteristics of oxygen concentration and regeneration temperature effect on continuous pulsation regeneration in diesel particulate filter for heavy-duty truck, Energy. 264 (2023) 126265.

[8] D. Wang, J. Cao, P. Tan, Z. Wang, W. Li, Z. Liu, J. Wang, Full course evolution characteristics of DPF active regeneration under different inlet HC concentrations, Fuel. 310 (2022) 122452.

[9] M. Yu, D. Luss, V. Balakotaiah, Analysis of flow distribution and heat transfer in a diesel particulate filter, J. Chem. Eng. 226 (24) (2013) 68–78.

[10] J. Fang, Z. Meng, J. Li, Y. Du, Y. Qin, Y. Jiang, W. Bai, G.G. Chase, The effect of operating parameterson regeneration characteristics and particulate emission characteristics of diesel particulate filters, Appl. Therm. Eng. 148 (2019) 860–867.

[11] S.J. Lee, S.J. Jeong, W.S. Kim, Numerical design of the diesel particulate filter for optimum thermal performances during regeneration, Appl. Energy. 86 (7) (2009) 1124–1135.

[12] J.R. Serrano, F.J. Arnau, P. Piqueras, O.G. Afonso, Packed bed of spherical particles approach for pressure drop prediction in wall-flow DPFs (diesel particulate filters) under soot loading conditions, Energy. 58 (2013) 644–654.

[13] Z. Meng, J. Li, J. Fang, J. Tan, Y. Qin, Y. Jiang, Z. Qin, W. Bai, K. Liang, Experimental study on regeneration performance and particle emission characteristics of DPF with different inlet transition sections lengths, Fuel. 262 (2020) 116487.

[14] Z. Meng, C. Chen, J. Li, J. Fang, J. Tan, Y. Qin, Y. Jiang, Z. Qin, W. Bai, K. Liang, Particle emission characteristics of DPF regeneration from DPF regeneration bench and

diesel engine bench measurements, Fuel. 262 (2020) 116589.

[15] P. Tan, L. Dua, E. Li, Z. Hu, D. Lou, Experimental study on the temperature characteristics of a diesel particulate filter during a drop to idle active regeneration process, Appl. Therm. Eng. 178 (2022) 115628.

[16] C.T. Lao, J. Akroyd, N. Eaves, A. Smith, N. Morgan, A. Bhave, M. Kraft, Modelling particle mass and particle number emissions during the active regeneration of diesel particulate filters, Proc. Combust. Inst. 37 (2019) 4831–4838.

[17] K. Laziri, I. Lamara, F.Z. Mezahi, F. Sahnoune, E. Dhahri, S.F. Hassan, N. Saheb, Synthesis, microstructure, hardness, thermal expansion, and dielectric properties of cordierite, Int J Appl Ceram Technol. (2025) e15173.

[18] L.F. Nascimento, J.F. Lima, P.C. de Sousa Filho, O.A. Serra, Control of diesel particulate emission based on Ag/CeOx/FeOy catalysts supported on cordierite, J. Chem. Eng. 290 (2016) 454-464. https://doi.org/ 10.1016/j.cej.2016.01043.

[19] M. Valaskova, K.K. Kupkova, Cordierite/steatite/CeO_2 porous materials: Preparation, structural characterization and their photocatalytic activity, MICROPOR MESOPOR MAT 207 (2015) 120-125. https://doi.org/ 10.1016/j.micromeso.2014.12035.

[20] T. Luo, P. Li, W. Dong, Q. Zeng, X. Yu, X. Gu, G. Dong, Development of cordierite-based low-expansion porcelain tiles with application potential in an underfloor heating system, Int J Appl Ceram Technol. 22 (2025) e15031.

[21] G. Yan, L. Chen, Q. Jiang, L. Zhang, J. Wang, Y. Yang, Z. Li, J. Feng, Thermal/mechanical properties of cordierite synthesized using coal gangue as a

refractory material, Int J Appl Ceram Technol. 22 (2025) e14987.

[22] W. Xu, C. Kou, E. Jiaqiang, C. Feng, Y. Tan, Effect analysis on the flow uniformity and pressure drop characteristics of the rotary diesel particulate filter for heavy-duty truck, Energy. 288 (2024) 129820.

[23] L.F. Nascimento, R.F. Martins, R.F. Silva, O.A. Serra, Catalytic combustion of soot over ceria-zinc mixed oxides catalysts supported onto cordierite, J. Environ. Sci. 26 (2014) 694-701. https://doi.org/ 10.1016/S1001-0742(13)60442-8.

[24] J. Wei, C. Fan, D. Li, Y. Zhuang, Z. Fu, Z. Guan, H. Li, D. Li, Y. Qian, Diesel soot combustion over ceria catalyst: Evolution of functional groups on soot surfaces, Fuel. 338 (2023) 127391. https://doi.org/ 10.1016/j.fuel.2023.127391.

[25] Z. Shi, Y. Liu, W. Yang, K. Liang, F. Pan, S. Gu, Evaluation of cordierite–ceria composite ceramics with oxygen storage capacity, J. Eur. Ceram. Soc. 22 (2002) 1251-1256.

[26] S. Zeng, A. Shui, H. Yu, C. He, Sonochemical synthesis of CeO_2 nanoparticles with high photocatalytic and antibacterial activities under visible light, Int J Appl Ceram Technol. 21 (2024) 3141–3151.

[27] S. Liu, Y. Zeng, D. Jiang, Effects of CeO_2 addition on the properties of cordierite-bonded porous SiC ceramics, J. Eur. Ceram. Soc. 29 (2009) 1795-1802. https://doi.org/ 10.1016/j.jeurceramsoc.2008.11002.

[28] S. Bensaid, N. Russo, D. Fino, CeO_2 catalysts with fibrous morphology for soot oxidation: The importance of the soot–catalyst contact conditions, Catal. Today. 216 (2013) 57–63.

548 [29] M. Zhang, Y. Wang, M. Yu, M. He, L. Cao, X. Luo, W. Wang, Preparation of
549 aluminum borate whiskers/CoxCr3-xO4 catalysts on channel surface of cordierite
550 honeycomb ceramic for soot catalytic combustion, Int J Appl Ceram Technol. 22 (2025)
551 e14994.
552 [30] Y. Liu, C. Su, J. Clerc, A. Harinath, L. Rogoski, Experimental and modeling study
553 of ash impact on DPF backpressure and regeneration behaviors, SAE. Int. J. Engines.
554 8 (3) (2015) 1313–1321.
555 [31] Han Yan, Ningqiang Zhang, Dingsheng Wang, Highly efficient CeO_2-supported
556 noble-metal catalysts: From single atoms to nanoclusters, Chem. Catalysis. 2 (2022)
557 1594–1623.
558 [32] Y. Jin, N. Shinoda, Y. Uesaka, T. Kuki, M. Yamashita, H. Sakamoto, C.D. Vogt,
559 Development of new high porosity diesel particulate filter for integrated
560 SCRtechnology/catalyst, SAE. Int. J. Fuels. Lubr. 8 (2015) 494–500.
561 [33] F. Sandra, A. Ballestero, V.L. Nguyen, M.N. Tsampas, P. Vernoux, C. Balan, Y.J.
562 Iwamoto, U.B. Demirci, P. Miele, S. Bernard, Silicon carbide-based membranes with
563 high soot particle filtration efficiency, durability and catalytic activity for CO/HC
564 oxidation and soot combustion, J. Membr. Sci. 50 (2016) 79-92. https://doi.org/
565 10.1016/j.memsci.2015.12015.
566 [34] M.P. Orihuela, O. Haralampous, R. Chacartegui, M.T. García, J. Martínez-
567 Fernández, Numerical Simulation of a Wall-Flow Particulate Filter Made of
568 Biomorphic Silicon Carbide Able to Fit Different Fuel/Biofuel Inputs, Processes. 7
569 (2019) 945. https://doi.org/ 10.3390/pr7120945.

570 [35] F. Fang, P. Zhao, N. Feng, H. Wan, G. Guan, Surface engineering on porous
571 perovskite-type $La_{0.6}Sr_{0.4}CoO_3$-δ nanotubes for an enhanced performance in diesel soot
572 elimination, J. Hazard. Mater. 399 (2020) 2–12.
573 [36] C. Zhang, D. Yu, C. Peng, L. Wang, X. Yu, Y. Wei, J. Liu, Z. Zhao, Research
574 progress on preparation of 3DOM-based oxide catalysts and their catalytic
575 performances for the combustion of diesel soot particles, Appl. Catal. B. 319 (2022) 2–
576 27.
577 [37] H.J. Guo, Q.L. Li, H.R. Zhang, F. Peng, L. Xiong, S.M. Yao, C. Huang, X.D.
578 Chen, CO_2 hydrogenation over acid-activated Attapulgite/$Ce_{0.75}Zr_{0.25}O_2$
579 nanocomposite supported Cu-ZnO based catalysts, Mol. Catal. 476 (2019) 110499.
580 https://doi.org/ 10.1016/j.mcat.2019.110499.
581 [38] H.J. Guo, H.R. Zhang, F. Peng, H.J. Yang, L. Xiong, C. Huang, C. Wang, X.D.
582 Chen, L.L. Ma, Mixed alcohols synthesis from syngas over activated palygorskite
583 supported Cu-Fe-Co based catalysts, Appl. Clay. Sci. 111 (2015) 83-89. https://doi.org/
584 10.1016/j.clay.2015.03009.
585 [39] J. Cao, G. Shao, Y. Wang, Y. Liu, Z. Yuan, CuO catalysts supported on attapulgite
586 clay for low-temperature CO oxidation, Catal. Commun. 9 (2008) 2555-2559.
587 https://doi.org/ 10.1016/j.catcom.2008.07016.
588 [40] C. Zhu, X. Wang, Q. Huang, L. Huang, J. Xie, C. Qing, T. Chen, Removal of
589 gaseous carbon bisulfide using dielectric barrier discharge plasmas combined with TiO_2
590 coated attapulgite catalyst, J. Chem. Eng. 225 (2013) 567-573. https://doi.org/
591 10.1016/j.cej.2013.03107.

592 [41] X. Li, H. Zhang, H. Lv, S. Zuo, Y. Zhang, C. Yao, Photo-assisted SCR removal of
593 NO by up conversion CeO_2/Pr^{3+}/attapulgite nanocatalyst, Environ. Sci. Pollut. Res. 26
594 (2019) 12842-12850.
595 [42] H. Yan, N. Zhang, D. Wang, Highly efficient CeO_2-supported noblemetal catalysts:
596 From single atoms to nanoclusters. Chem Catalysis 2(7) (2022) 1594-623.
597 [43] X. Deng, M. Li, J. Zhang, X. Hu, J. Zheng, N. Zhang, B. Chen, Constructing nano-
598 structure on silver/ceria-zirconia towards highly active and stable catalyst for soot
599 oxidation, J. Chem. Eng. 313 (2017) 544-555. https://doi.org/ 10.1016/j.cej.2016.12088.
600 [44] Z. Meng, Z. Bao, Z. Chen, B. Zeng, Z. Qin, J. Tan, P. Pu, Experimental effects of
601 ash (ZnO) and catalyst (CeO_2) on DPF regeneration performance and emission
602 characteristics. Fuel 365 (2024) 131193.
603 [45] J. Ou, Z. Meng, Y. Hu, Y. Du, Experimental investigation on the variation
604 characteristics of soot layer thickness and pressure drop during DPF/CDPF active
605 regeneration. Chem. Eng. Sci. 241 (2021) 116682.
606 [46] A. Bueno-López, Diesel soot combustion ceria catalysts, Appl. Catal. B. Environ.
607 146 (2014) 1-11. https://doi.org/ 10.1016/j.apcatb.2015.12030.
608 [47] D. Fino, S. Bensaid, M. Piumetti, N. Russo, A review on the catalytic combustion
609 of soot in diesel particulate filters for automotive applications: From powder catalysts
610 to structured reactors, Appl. Catal. A. Gener. 509 (2016) 75-96. https://doi.org/
611 10.1016/j.apcata.2015.10016.
612 [48] B. Zhao, X. Liang, K. Wang, T. Li, X. Lv, S. Zhang, Impact of sulfur functional
613 groups on physicochemical properties and oxidation reactivity of diesel soot particles,

614 Fuel. 327 (2022) 125041. https://doi.org/ 10.1016/j.fuel.2022.125041.

615 [49] J. Wei, C. Fan, L. Qiu, Y. Qian, C. Wang, Q. Teng, M. Pan, Impact of methanol

616 alternative fuel on oxidation reactivity of soot emissions from a modern CI engine, Fuel.

617 268 (2020) 117352.

618 [50] E. Aneggi, V. Rico-Perez, C. de Leitenburg, S. Maschio, L. Soler, J. Llorca, A.

619 Trovarelli, Ceria-zirconia particles wrapped in a 2D carbon envelope: Improved low-

620 temperature oxygen transfer and oxidation activity. Angew. Chem. Int. Ed. 54 (2015)

621 14040-14043.

622 [51] Y. Wang, J. Wang, H. Chen, M. Yao, Y. Li. Preparation and NOx-assisted soot

623 oxidation activity of a CuO-CeO_2 mixed oxide catalyst. Chemical Engineering Science,

624 135 (2015) 294–300.

625 [52] J. Neeft, M. Makkee, J.A. Moulijn, Catalysts for the oxidation of soot from diesel

626 exhaust gases I An exploratory study, Appl. Catal. B. Environ. 8 (1) (1996) 57-78.

627 [53] X. Liang, Y. Wang, K. Wang, Y. Wang, H. Zhang, B. Zhao, X. Lv, Experimental

628 study of impact of lubricant-derived ash on oxidation reactivity of soot generated in

629 diesel engines, Proc Combust Inst 38(4) (2021) 5635–5642.

630 [54] S. Wagloehner, M. Nitzer-Noski, S. Kureti, Oxidation of soot on manganese oxide

631 catalysts. Chem. Eng. J. 259 (2015) 492–504.

632 [55] T. Andana, M. Piumetti, S. Bensaid, N. Russo, D. Fino, R. Pirone, Nanostructured

633 ceria-praseodymia catalysts for diesel soot combustion, Applied catalyst, Appl. Catal.

634 B. Environ. 197 (2016) 125-137. https://doi.org/ 10.1016/j.apcatb.2015.12030.

635 [56] J. She, T. Ohji, Fabrication and characterization of highly porous mullite ceramics,

636 Mater. Chem. Phys. 80 (2003) 610–614.

637 [57] F. Yang, C. Li, Y. Lin, C.-A. Wang, Effects of sintering temperature on properties

638 of porous Mullite/Corundum ceramics, Mater. Lett. 73 (2012) 36–39.

639 [58] Y. Wang, X. Liang, G. Tang, Y. Chen, L. Dong, G. Shu, Impact of lubricating oil

640 combustion on nanostructure, composition and graphitization of diesel particles, Fuel

641 190 (2017) 237-244.

642 [59] Y. Wang, X. Liang, K. Wang, Y. Wang, L. Dong, G. Shu, Effect of base oil on the

643 nanostructure and oxidation characteristics of diesel particulate matter, Appl. Therm.

644 Eng. 106 (2016) 1311-1318.

645 [60] Y. Liu, X. Zhang, G. Lyu, Y. Qiao, W. Zhang, C. Song, Effect of the oxidation-

646 induced fragmentation of primary particles on soot oxidation reactivity, Combust.

647 Flame. 240 (2022) 112026. https://doi.org/ 10.1016/j.combustflame.2022.112026.

648 [61] X. Liang, Y. Wang, Y. Wang, B. Zhao, Z. Zhang, X. Lv, Z. Wu, X. Cai, K. Wang,

649 Impact of lubricating base oil on diesel soot oxidation reactivity, Combust. Flame. 217

650 (2020) 77-84. https://doi.org/ 10.1016/j.combustflame.2020.03035.

651 [62] Y. Wang, H. Yang, X. Liang, H. Song, Z. Tao, Effect of lubricating base oil on the

652 oxidation behavior of diesel exhaust soot, Sci. Total. Environ. 858 (2023) 160009.

653 https://doi.org/ 10.1016/j.scitotenv.2022.160009.

654 [63] Y. Liu, C.X. Fan, F. Wang, H. Liu, Chen, Thermally induced variations in the

655 nanostructure and reactivity of soot particles emitted from a diesel engine,

656 Chemosphere. 286 (2022) 131712.

657 [64] D. Dollimore, T.A. Evans, Y.F. Lee, F.W. Wilburn, Correlation between the shape

658 of a TG/DTG curve and the form of the kinetic mechanism which is applying,
659 Thermochim. Acta. 198 (2) (1992) 249–257.
660 [65] J. Neeft, T.X. Nijhuis, E. Smakman, S. Erik, M. Michiel, J.A. Moulijn, Kinetics of
661 the oxidation of diesel soot, Fuel. 76 (12) (1997) 1129–1136.
662 [66] V. Palma, P. Ciambelli, E. Meloni, A. Sin, Study of the catalyst load for a
663 microwave susceptible catalytic DPF, Catal. Today. 216 (2013) 185-193.
664 https://doi.org/ 10.1016/j.cattod.2013.07012.
665 [67] Y.H. Yu, J.C.S. Wu, Removal of NOx by photocatalytic processes, J. Photochem
666 Photobiol. C: Photochem. Rev. 14 (2013) 29-52. https://doi.org/
667 10.1016/j.jphotochemrev.2012.08002.
668 [68] Z. Zhang, W. Wang, Y. Kang, L. Zong, A. Wang, Tailoring the properties of
669 palygorskite by various organic acids via a one-pot hydrothermal process: A
670 comparative study for removal of toxic dyes. Appl. Clay Sci. 120 (2016) 28-39.
671 [69] Z. Chen, F. Chen, X. Li, X. Lu, C. Ni, X. Zhao, Facile synthesis of CeO_2 nanotubes
672 templated by modified attapulgite, J. Rare. Earths. 28 (4) (2010) 566-570.
673 https://doi.org/ 10.1016/S1002-0721(09)60155-1.
674 [70] M. Gu, Q. Huang, L. Xu, J. Zhu, Y. Sun, T. Tao, B. Yang, M. Chen, H. Yang,
675 Improved activity and stability for chlorobenzene oxidation over ternary Cu-Mn-O-Ce
676 solid solution supported on cordierite, Environ. Sci. Pollut. Res. 30 (2023) 37535-
677 37546. https://doi.org/ 10.1007/s11356-022-24988-1.
678 [71] C. Russo, A. Ciajolo, Effect of the flame environment on soot nanostructure
679 inferred by Raman spectroscopy at different excitation wavelengths, Combust. Flame.

680 162 (2015) 2431-2441. https://doi.org/ 10.1016/j.combustflame.2015.02011.
681 [72] Y. Guo, Z. Ristovski, E. Graham, S. Stevanovic, P. Verma, M. Jafari, B. Miljevic,
682 R. Brown, The correlation between diesel soot chemical structure and reactivity,
683 Carbon. 161 (2020) 736-749. https://doi.org/ 10.1016/j.carbon.2020.01061.
684 [73] M. Lapuerta, F. Oliva, J.R. Agudelo, A.L. Boehman, Effect of fuel on thesoot
685 nanostructure and consequences on loading and regeneration of diesel particulate filters,
686 Combust. Flame. 159 (2012) 844-853. https://doi.org/
687 10.1016/j.combustflame.2011.09003.
688 [74] L. Wang, C. Song, J. Song, G. Lv, H. Pang, W. Zhang, Aliphatic C–H and
689 oxygenated surface functional groups of diesel in-cylinder soot: Characterizations and
690 impact on soot oxidation behavior, Proc. Combust. Inst. 34 (2) (2013) 3099–3106.

Dear editor and reviewers,

Thanks a lot for your time and valuable comments. We have now revised our manuscript according to these comments item by item. Below is our detailed reply.

Reviewer #1: In this paper, the effect of thermal oxidation on the morphological properties of cordierite (Cord) and attapulgite (ATP) was studied, and the results showed that the special fibrous or rod-like structure of ATP produced more pore volume and surface area, as well as a good heat recovery mechanism after thermal oxidation, broadened its application range as a catalyst substrate. The study contains some interesting findings that are valuable for understanding the structure of porous substrate materials in diesel particulate filter (DPF). As such, it has the potential to be published in the International Journal of Applied Ceramic Technology. However, the authors have to carefully implement the following comments in the revised manuscript before publication. I will give this paper a "minor revise". The specific comments are as follows:

1. In the introduction, the effect of the morphology of CeO_2 is proposed, and whether the CeO_2 used in this paper promotes solid-solid interaction.

Reply: *As proposed in introduction, the fibrous morphology is the best one for passive regeneration, which promoted solid–solid interaction [28]. In present study, the morphology of ATP shows special fibrous or rod-like structure. The solid–solid interactions between CeO_2 catalyst and soot particles are enhanced, promoting soot thermal catalytic reaction. The supplementary analysis has been added in revised manuscript (highlighted in red), which are listed below for your convenience. (line 426-428)*

"The solid–solid interactions between CeO2 catalyst and soot particles were enhanced by fibrous or rod-like structure of ATP, indicating more complete catalytic reaction."

[28] S. Bensaid, N. Russo, D. Fino, CeO_2 catalysts with fibrous morphology for soot oxidation: The importance of the soot–catalyst contact conditions, Catal. Today. 216 (2013) 57–63.

2. The author has repeatedly suggested that this material can be recycled many times. After several oxidation behaviors, does the structure and morphology of the material in this paper change? What is the cyclic stability of the material and the catalytic soot oxidation? Please add clarification.

Reply: *As suggested by the reviewer, the analysis of ATP and Cord substrate material cyclic stabilities and morphology changes are now added and listed below for the reviewer's convenience. (highlighted in red, line 401-415)*

"The SEM analysis of ATP revealed minor changes in the material's morphology microstructure. Before and after thermal oxidation, the irregularly arranged rod-shaped structures were always presented in ATP whiskers. Similarly, the block-like structure of Cord only acted as a substrate. The effect of thermal oxidation

on the block-like structure of Cord could almost be ignored. The XRD peak intensities of ATP characteristic peaks corresponding to (040) and (400) planes and Cord characteristic peaks corresponding to (110), (112) and (132) showed no changes after oxidized 50%, indicating better stability of crystalline structure. Meanwhile, the peak intensities of CeO_2 characteristic peaks had no changes before and after oxidation. To better evaluate the cyclic stability of substrate materials, the BET analysis was performed before and after thermal oxidation. The change rates of pore volume and pore diameter of Cord before and after thermal oxidation are less than 15%. Although the surface area of ATP decreased from 81.9 to 44.2 m^2/g, it is also significantly bigger than that of Cord. Therefore, in present study, both substrate materials of catalyst demonstrated superior stability. "

3. How are the soot samples used for FTIR and Raman spectroscopy analysis performed? Is there a pre-treatment process for particulate matter? How to remove the interference of filter paper, how to reduce the error? The test part needs to be explained.

Reply: *For Raman, FTIR and TGA analysis, the PM samples were collected by quartz fiber filters (2500QRT-UP, PALL,47 mm) with automized filter supporter. There were 2 hours or longer to get enough samples for further analysis. Subsequently, the particles attached to the filter paper surface were carefully scraped off from the paper filters. During this process, the filter paper was guaranteed not to be damaged, and the interference of filter paper could be removed. For avoiding moisture atmosphere, the samples were stored in a desiccator. There were no pre-treatment processes for soot particles, like ultrasonic wave treatment and centrifugal separation in dichloromethane solvent (removing VOF) [49]. This is because the particle samples analyzed in this study are not dry soots, which is employed for mimicking the real state of PM in DPF filter. This paragraph* **is added in revised manuscript** *(highlighted in red),* **which are listed below for your convenience. (line 133-144)**

"Soot particles were collected from the raw exhaust using 47 mm quartz fiber filters (2500QRT-UP, PALL) equipped with an automated filter support. The quartz fiber filters exhibited a precision of 0.3 µm with an aerosol retention rate of 99.9%. The sampling temperature was maintained at 55 ± 3 °C, with sampling duration of 90 min and sample flow rate of 1 L/s. In order to get enough samples for further analysis, the sampling time was controlled at 2 hours or longer. Subsequently, the particles attached to the filter paper surface were carefully scraped off from the paper filters. During this process, the filter paper was guaranteed not to be damaged, and the interference of filter paper could be removed. To prevent atmospheric moisture from affecting the samples, the soot particle samples were stored in a desiccator after each measurement [48]. There pre-treatments like ultrasonic wave treatment and centrifugal separation in dichloromethane solvent were not employed in this study [49]."

[49] J. Wei, C. Fan, L. Qiu, Y. Qian, C. Wang, Q. Teng, M. Pan, Impact of methanol alternative fuel on oxidation reactivity of soot emissions from a modern CI engine, Fuel. 268 (2020) 117352.

4. Why did thermal treatment program in Table 2 was chosen?

Reply: *The VOF, which was mainly consisted of OC (organic carbon), could be removed by thermal treatment [58,59]. In this study, soot particles were heated from 25 ℃ to 450 ℃ and keeping it adiabatic for 30 min by employing high-purity nitrogen as protective gas. The mass loss was from organic thermal decomposition of organic compounds. This explanation has been supplemented and highlighted in red which are listed below for your convenience. (line 182-185)*

"The volatile organic fraction, which was mainly consisted of organic carbon, could be removed by thermal treatment [58,59]. To remove organic carbon, the soot particle sample was heated to 450 °C and then maintained for 30 min, utilizing high-purity nitrogen as protective gas."

[58] Y. Wang, X. Liang, G. Tang, Y. Chen, L. Dong, G. Shu, Impact of lubricating oil combustion on nanostructure, composition and graphitization of diesel particles, Fuel 190 (2017) 237-244.

[59] Y. Wang, X. Liang, K. Wang, Y. Wang, L. Dong, G. Shu, Effect of base oil on the nanostructure and oxidation characteristics of diesel particulate matter, Appl. Therm. Eng. 106 (2016) 1311-1318.

5. Can superposing Ce dispersion images onto their corresponding SEM images provide more precise information?

Reply: *The Ce dispersion of samples onto their corresponding SEM images have been provided below. Obviously, comparing with Fig. 4, it is more difficult to find the discrepancy in Ce dispersion. Therefore, the original figure of elemental mapping for catalyst/substrate samples should be preserved.*

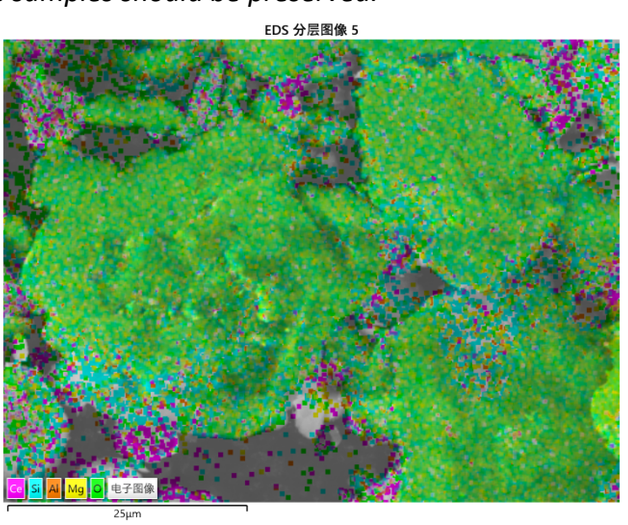

ATP200/CeO_2

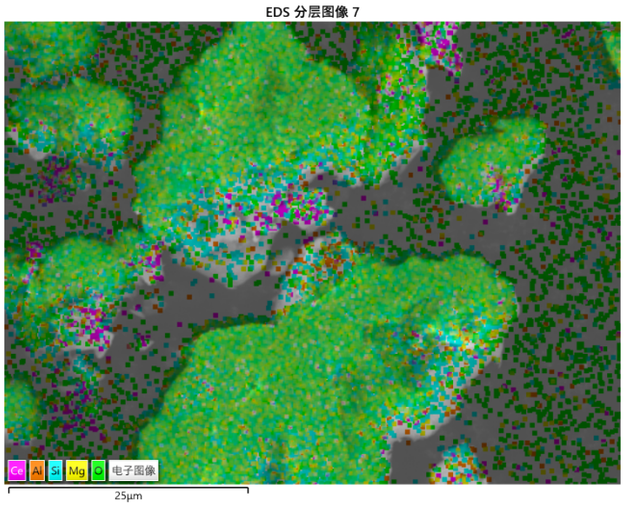

Cord200/CeO_2

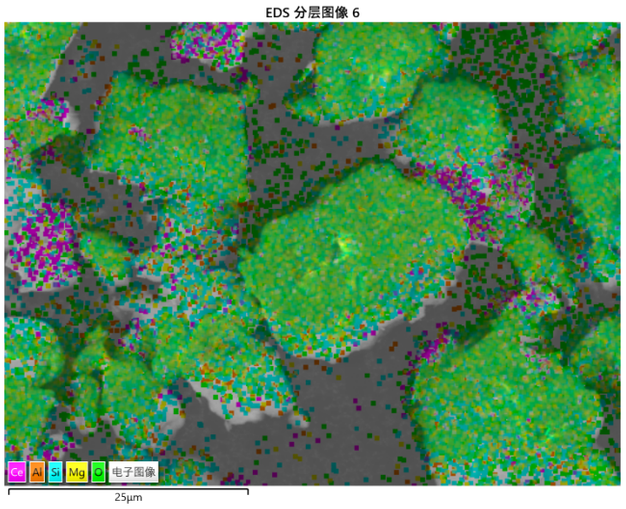

ATP325/CeO_2

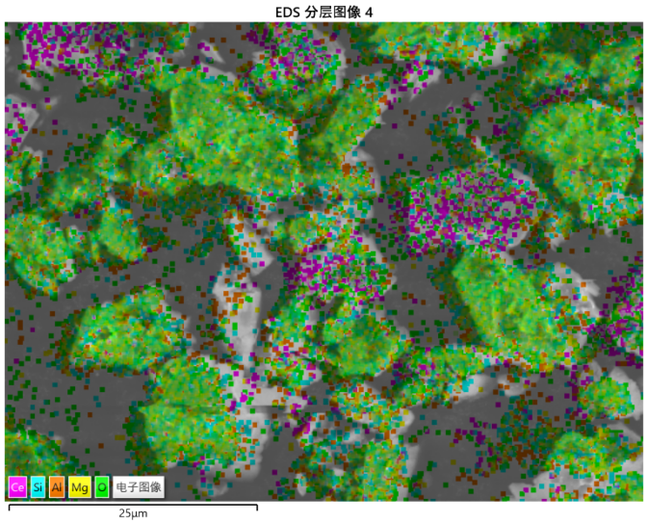

Cord 325/CeO_2

6. There are two legends of “Cord200/CeO2/Soot” in Fig.7 (c) and (d), please check.
Reply: *The legend of* Fig.7 (d) *has been revised as follows.*

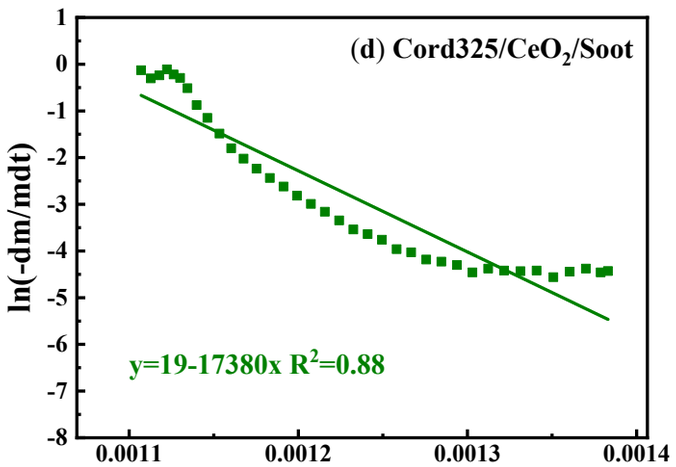

Reviewer #2: ***Comments to the Author***
1. In the introduction section, please add some latest references, such as (International Journal of Applied Ceramic Technology, http://doi.org/10.1111/ijac.14994).
Reply: *Thanks. The literatures suggested by reviewer are now added during the discussion in revised manuscript (highlighted in red), which are listed below for your convenience.*

“Zeng et al. [26] found that CeO_2 nanoparticles could provide a higher surface area without any heat treatment.” (line 62-63)
[26] S. Zeng, A. Shui, H. Yu, C. He, Sonochemical synthesis of CeO_2 nanoparticles with high photocatalytic and antibacterial activities under visible light, Int J Appl Ceram Technol. 21 (2024) 3141–3151.

“It was reported that the Cord is known to form at high temperature sintering method, which has a dense microstructure with evenly distributed grains and few small pores [17]. “(line 54-56)
[17] K. Laziri, I. Lamara, F.Z. Mezahi, F. Sahnoune, E. Dhahri, S.F. Hassan, N. Saheb, Synthesis, microstructure, hardness, thermal expansion, and dielectric properties of cordierite, Int J Appl Ceram Technol. (2025) e15173.

“The Cord had favorable thermal expansion coefficient and resistance to cracking from material fatigue, and an excellent thermal shock resistance [17-21].” (line 56-57)
[20] T. Luo, P. Li, W. Dong, Q. Zeng, X. Yu, X. Gu, G. Dong, Development of cordierite-based low-expansion porcelain tiles with application potential in an underfloor heating system, Int J Appl Ceram Technol. 22 (2025) e15031.
[21] G. Yan, L. Chen, Q. Jiang, L. Zhang, J. Wang, Y. Yang, Z. Li, J. Feng,

Thermal/mechanical properties of cordierite synthesized using coal gangue as a refractory material, Int J Appl Ceram Technol. 22 (2025) e14987.

"Zhang er al. [29] suggested that aluminum borate whiskers with cilia-like microstructure improved soot capture ability and low-temperature catalytic oxidation ability of soot. "(line 69-71)
[29] M. Zhang, Y. Wang, M. Yu, M. He, L. Cao, X. Luo, W. Wang, Preparation of aluminum borate whiskers/CoxCr3-xO4 catalysts on channel surface of cordierite honeycomb ceramic for soot catalytic combustion, Int J Appl Ceram Technol. 22 (2025) e14994.

2. How is the cycling stability of the catalyst?
Reply: *The cycling stability of the catalyst can be evaluated by analysis of SEM, XRD and BET. The SEM analysis of ATP revealed minor changes in the material's morphology microstructure. Before and after thermal oxidation, the irregularly arranged rod-shaped structures were always presented in ATP whiskers. Similarly, the block-like structure of Cord only acted as a substrate. The effect of thermal oxidation on the block-like structure of Cord could almost be ignored. The XRD peak intensities of ATP characteristic peaks corresponding to (040) and (400) planes and Cord characteristic peaks corresponding to (110), (112) and (132) showed no changes after oxidized 50%, indicating better stability of crystalline structure. Meanwhile, the peak intensities of* CeO_2 *characteristic peaks had no changes before and after oxidation. To better evaluate the cyclic stability of substrate materials, the BET analysis was performed before and after thermal oxidation. The change rates of pore volume and pore diameter of Cord before and after thermal oxidation are less than 15%. Although the surface area of ATP decreased from 81.9 to 44.2* m^2/g*, it is also significantly bigger than that of Cord. Therefore, in present study, both substrate materials of catalyst demonstrated superior stability. The supplementary analysis has been added in revised manuscript (highlighted in red), which are listed below for your convenience. (line 401-415)*